Flexibility Enhancement of Flexible Solar Cell Devices by Nano-Mechanical Analysis of The Constituent Materials

Jeong-Hyun Woo

Department of Materials Science and Engineering

Graduate School of UNIST

Flexibility Enhancement of Flexible Solar Cell Devices by Nano-Mechanical Analysis of The Constituent Materials

A thesis/dissertation
submitted to the Graduate School of UNIST
in partial fulfillment of the
requirements for the degree of
Doctor of Philosophy

Jeong-Hyun Woo

06. 10. 2020
Approved by

_____

Advisor
Prof. Ju-Young Kim

Flexibility Enhancement of Flexible Solar Cell Devices by Nano-Mechanical Analysis of The Constituent Materials

Jeong-Hyun Woo

This certifies that the dissertation of Jeong-Hyun Woo is approved.

06. 10. 2020

signature

_____

Advisor: Prof. Ju-Young Kim

signature

_____

Prof. Myoung Hoon Song

signature

_____

Prof. Han Gi Chae

signature

_____

Prof. Eun-chae Jeon

signature

_____

Prof. Seung-Kyun Kang

Abstract

Recently, the research on flexible solar cells have been widely reported, and among them, mechanical flexibility is important to improve the stability and reliability of devices. Flexible solar cell can be classified by inorganic solar cell and organic solar cell. Among inorganic solar cell, silicon solar cells are achieved high power conversion efficiency over 25%, however, flexibility is limited by the catastrophic failure of silicon substrate. In case of organic solar cell, they have excellent flexibility, but efficiency decreases in the air due to their low stability.

Ultra-thin silicon has been used in flexible solar cell due to poor flexibility of silicon substrate. To reduce its high reflectance, it is necessary to introduce surface texturing on the bare silicon substrate. Silicon substrates are usually textured by two kinds of processes: anti-reflective coating and fabrication of a nano- or microstructure on surface. However, the results of the latter process, such as dome, pyramid, or pillar structures, can play the role of nano- or micro-flaws on the surface of the silicon substrate, leading to crack propagation and reducing the mechanical properties of the entire product. Thus, assessment of their structural integrity is critical in mechanical behavior and performance. In this study, we measured flexural strength and bending radius of ultra-thin textured silicon using 4-point bending tests. We explained the effect of textured structures on the flexural strength of ultra-thin silicon samples by using a Weibull distribution. Failure analysis also was carried out from SEM images of the fracture surfaces and FEA simulations.

Amorphous inorganic thin films are used for moisture-diffusion barriers due to their excellent resistance to moisture. To improve the reliability of organic solar cell, flexibility of inorganic barrier film has to be improved to maintain the encapsulation performance after repeated deformation. By Griffith's theory, the fracture strength of brittle materials reaches a theoretical strength at a critical thickness. In this study, mechanical properties of amorphous Al_2O_3 thin films were measured by in-situ tensile tests and critical bending radius was calculated based on tensile results. Also, water vapor transmission rate of Al_2O_3 thin films was measured by electrical calcium test and cyclic bending tests were performed for reliability evaluation.

Contents

List of Figures

List of Tables

1. Introduction

The serious environmental problems, such as global warming, are caused by increased CO_2 gas from the use of conventional energy sources (such as coal fuel and fossil fuels), therefore, research on alternative energy is important assignment in the world [1-3]. Among the alternative energy, solar energy is largest and sustainable energy source [4], and high-power conversion efficiency has been achieved for silicon-based solar cell [5]. However, it is insufficient for flexible solar cell due to rigidity of substrate. Flexible solar cell can be classified by inorganic based solar cells and organic based solar cells. Inorganic based solar cells have high stability [6] and efficiency, but their flexibility is limited by the catastrophic failure of inorganic materials [7-9]. Meanwhile, advantages of organic based solar cells are excellent flexibility and light weight, but efficiency degrades due to low stability of organic materials under ambient condition [10, 11].

Silicon solar cell is the representative of inorganic solar cell, and have high efficiency, but low flexibility [7-9] and relatively high cost of process and materials [12, 13]. To improve the flexibility, ultra-thin silicon substrates are used in solar cells [14-16]. When bending deformation is applied to materials, tensile and compressive deformation are generated at top and bottom of neutral plane, respectively. The farther from the neutral plane, the more stress is applied to the surface, therefore the use of ultra-thin silicon improves the flexibility of the silicon solar cell. Ultra-thin silicon has the advantage of not only improving flexibility, but also reducing cost by reducing the silicon thickness, which occupies the most cost in silicon solar cells [12, 17]. Since optical reflectance of silicon is high, surface texturing process is required to reduce the reflectance. The anti-reflection and light trapping effects of surface texturing increase the efficiency of surface textured solar cells compared to planar surface [18, 19]. Also, surface textured solar cell shows more stable efficiency results than non-textured solar cell after cyclic bending [20]. However, surface texture can act as a stress concentrator as surface defect and can affect strength and flexibility [7, 21]. Analysis of mechanical properties depending on surface texturing is very important.

The organic based solar cells are sensitive to water vapor and oxygen, and power conversion efficiency degrades under ambient condition [10, 11]. Encapsulation is required to prevent the device from being exposed to moisture [22-24]. High transparency, flexibility and low permeability are condition of encapsulation material. Encapsulation materials need to be transparent so that all the light from the sun can pass through it. The encapsulation materials are usually formed by inorganic materials such as glass and thick-metal foil [25]. However, glass is insufficient for flexible device due to rigidity and metal foil is not suitable for solar cell due to low transparency [26]. Therefore, transparent oxide layers are used as a thin film encapsulation method for flexible encapsulation [27, 28]. Brittle behavior of oxide glass is major problem in commercialization. As mentioned earlier, measurement of

mechanical properties of brittle materials is important for flexible devices and encapsulation. In this study, we analyzed the flexibility of silicon substrate and inorganic encapsulation material used in flexible devices.

In chapter 3, flexural strength and critical bending radius of non-, dome- and pyramid textured silicon are measured by 4-point bending tests in OM system. Measured flexural strength is statistically analyzed by Weibull distribution and stress concentration is analyzed by theoretical equation and FEA simulation.

In chapter 4, mechanical properties and moisture permeability of Al_2O_3 thin films were measured by tensile test and electrical calcium test, respectively. Based on tensile results, critical bending radius was calculated, and cyclic bending was performed at a radius greater than critical bending radius. WVTR degradation mechanism at radius greater than critical bending radius is suggested. In addition, Al_2O_3 was applied to perovskite solar cell and encapsulation performance was evaluated by accelerated test.

2. Research background

2.1. Flexibility of ultra-thin silicon solar cell

2.1.1. Flexible ultra-thin silicon

Among the various types of inorganic solar cells, crystalline silicon (Si) solar cells are widely used due to their high energy-conversion efficiency and application feasibility. However, bulk silicon wafer has limitation for flexible solar cell due to lack of flexibility and high cost. To improve these disadvantages, ultra-thin silicon solar cells with a typical wafer thickness less than 100 um, which are flexible and possess the advantages of silicon solar cells, have been developed [15, 29]. The reduction of the silicon thickness results in production of low-cost flexible silicon solar cell [12]. The loss of efficiency occurs due to low light absorbance of silicon substrate. Surface texturing process has been widely used to reduce reflectivity and enhance light-trapping efficiency. When the light reaches the surface of silicon, it is divided into reflectance and absorbance. In planar surface, efficiency is limited due to loss of light absorbance. The surface texturing is that surface roughness is controlled by wet or dry etching (i.e. pyramidal and dome structure) and light absorbance increases through several surface reflectance [30]. In textured surface, light is repeatedly reflected by surface roughness and absorbance is improved. The planar surface silicon has ~40% reflectivity, however, textured silicon has ~10% reflectivity due to surface texturing [31].

The texturing methods can be classified by dry and wet etching. The wet etching process is a method that uses anisotropic etch rate depending on crystallographic orientation by a mixed solution such as KOH, NaOH and IPA. The etch rate can be controlled by temperature and solution mix ratio. The wet etching method has high etch rate and low cost, however, etch rate highly depends on temperature [32, 33]. The dry etching method typically uses RIE (Reactive Ion Etching) process which uses silicon etch gas such as SF_6 and O_2. In dry etching method, hard mask layer which partially covers the silicon surface is necessary to prevent the exposure of silicon. This method is not dependent on orientation and uniform texture can be fabricated by controlling gas ratio and pressure [34-36].

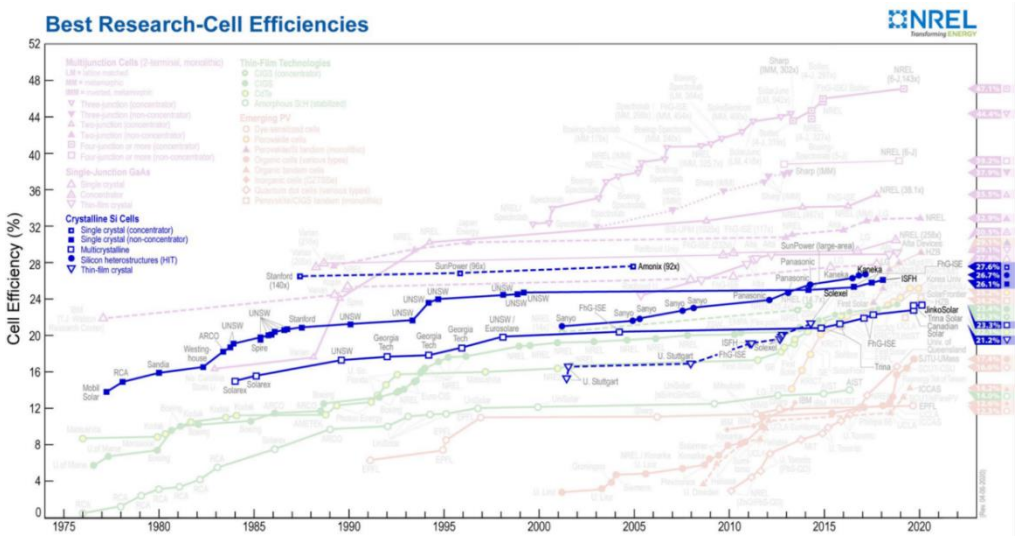

Figure 2-1. Best research-cell efficiency chart. Copy right 2020. NREL

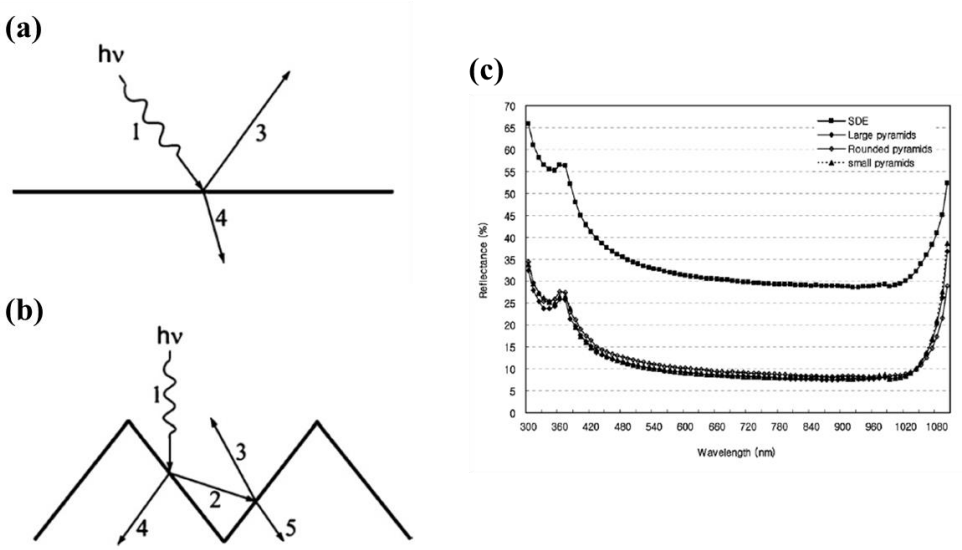

Figure 2-2. The surface texturing effect (a) Planar surface (b) Textured surface [30] (c) Reflectance of various surface texturing [31]

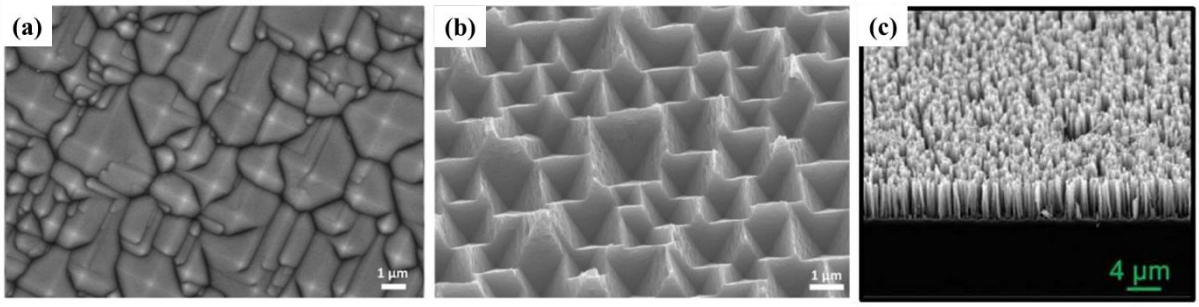

Figure 2-3. Surface texturing (a) Upright pyramid (b) Inverted pyramid [37] (c) Nanotexture pillar [38]

2.1.2. Mechanical properties of surface textured silicon

The ceramic materials such as silicon substrate has brittle and catastrophic failure. These materials are sensitive to surface and inside defects. Therefore, the surface textures in silicon wafers act as stress concentrators for mechanical deformation, which can reduce the flexibility of thin silicon solar cells. When a silicon wafer has a single notch, surface texturing in a fine and periodic array enhances the flexural strength of the silicon wafer because the stress concentration at the large notch is effectively dispersed by the surface texturing [38]. The mechanical behavior of thin single-crystalline silicon wafers with surface texturing strongly depends on the shape, scale, and distribution of the textured patterns; therefore, investigating the effects of surface texturing on the flexibility of ultra-thin silicon wafers are highly required.

Based on previous research [31], flexural strength of textured silicon is lower than planar surface silicon. However, as-saw silicon has lower value compared with textured silicon. It means that surface defects from wafer sawing process are weakest point when bending stress is applied. After saw damage etching using KOH solution, surface damage reduces result in flexural strength is improved owing to reduced stress concentrator. In case of pyramid textured silicon, flexural strength decreases as pyramid size increases because stress concentrates on valley of pyramid. After rounded process, because stress concentration is reduced by rounded tip, strength is improved. As a result, flexural strength is dependent on length and tip radius of surface texture.

Meanwhile, flexural strength of the nano-textured silicon is higher than planar surface silicon. Kashyap et al. [38] reported flexural strength of nano-textured silicon samples are measured using three-point bending test and have higher value than planar samples even including micro V-notch. The V-notch size is 2, 7 and 14 um and nano-textures are fabricated by wet-chemical etching with 100 nm-pitch and width. As a result of experiments and simulation, stress is concentrated on the notch tip in V-notch samples, however, stress is distributed in the nano-texture region. As nano-texture depth increases, stress distribution is enhanced and flexural strength from three-point bending test is improved. The depth of pre-existing manufacturing defect is 1~8 um, therefore, flexural strength of planar silicon is lower than nano-textured silicon owing to stress distribution i.e., strength of silicon wafer can be enhanced using nano-texturing.

To investigate the flexibility, bending tests typically are performed. The bending tests are classified by three-point bending test and four-point bending test. When the bending stress is applied for sample, outer line (neutral plane upper line) undergoes tensile stress and crack propagates. In case of three-point bending test, sample is loaded on two support rods and loading rod is located at centerline between support rods. In near loading rod, highest tensile stress is applied, therefore, flexural strength and flexibility is highly sensitive to surface defects closest to the centerline. In four-point bending test,

loading span is half of support span and loading rods are located equally from the centerline, respectively. The highest tensile stress is constant in the region between loading rods. Thus, four-point bending test is more sensitive to sample sidewall defects compared to three-point bending test. As a result, fracture strength and standard deviation from the three-point bending test are higher than that of four-point bending test. The maximum stress from three-point bending test and four-point bending test can be calculated using Equation (1) and (2) respectively.

$$\sigma_{3PB} = \frac{3Pl}{2wh^2} \tag{1}$$

$$\sigma_{4PB} = \frac{3Pl}{4wh^2} \tag{2}$$

Where l is the support span, w and h are the sample width and thickness respectively, and P is the applied load [39, 40].

Min et al [41]. reported that fracture strength of silicon die from single crystalline silicon wafer increased as thickness of silicon die was reduced. They measured flexural strength of 100~300 um thick-silicon dies by 4-point bending test. Flexural strength increased linearly until the thickness decreased from 300 um to 150 um. However, flexural strength of 100 um thick-silicon die could not be measured because 100 um thick-silicon was more flexible than measurable range and did not break. In brittle material, stress concentrates on pre-existing flaws. Since bigger sample has higher probability of including defects, fracture strength is reduced by size effect. Due to flexibility, jig design of 4-point bending test is important for ultra-thin silicon wafer strength measurement.

The strength distribution of a brittle materials can be analyzed by statistical distribution called by Weibull distribution owing to high standard deviation. Based on experimental results, we can calculate the Weibull modulus and characteristic strength through Weibull distribution.

$$P(V_0) = \exp\left[-\left(\frac{\sigma}{\sigma_0}\right)^m\right] \tag{3}$$

$$\ln\left[\frac{1}{P(V_0)}\right] = \left(\frac{\sigma}{\sigma_0}\right)^m \tag{4}$$

$$ln ln\left[\frac{1}{P(V_0)}\right] = m(ln\sigma - ln\sigma_0) \tag{5}$$

Where $P(V_0)$ is the probability that the solid will survive, σ and σ_0 are applied stress and characteristic strength respectively, and m is the Weibull modulus. The Weibull modulus (m) means statistical variation of measured flexural strength, lower value of m is caused by larger variation. As m is close to zero, material will fail at any stress. Also, when m is close to infinity, material cannot fail at any stress under characteristic strength. Thus, the traditional ceramic materials have much lower Weibull modulus than metal materials. The characteristic strength means that strength of survival probability of 37% and it is mean value in Weibull distribution [42].

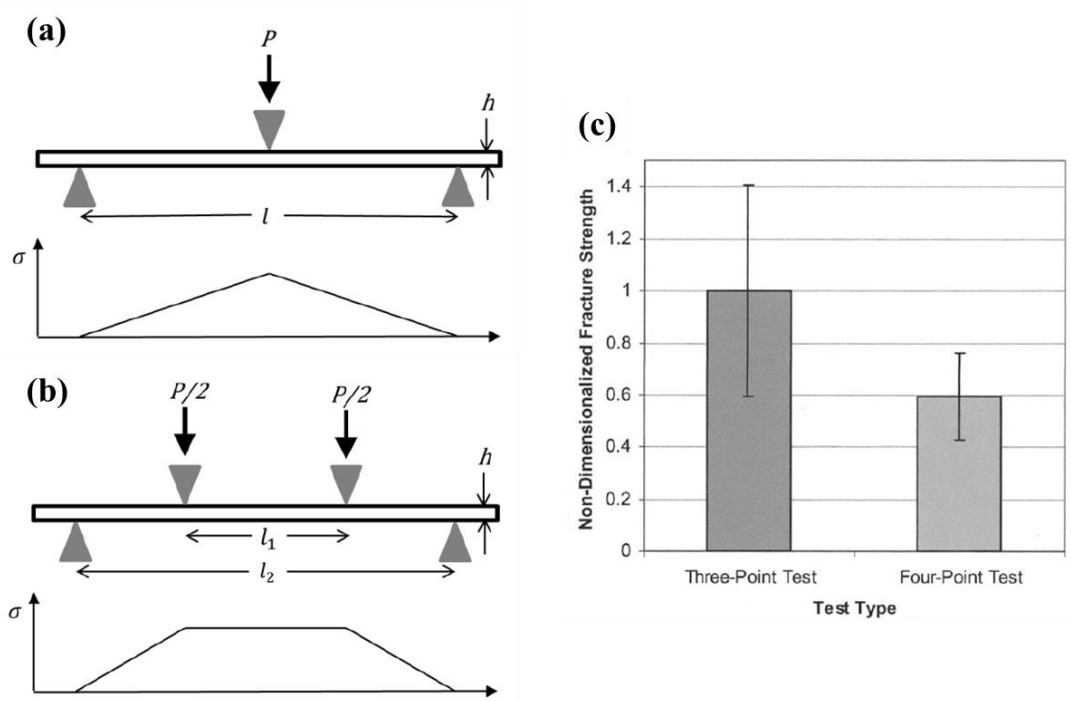

Figure 2-4. (a) 3-point bending test (b) 4-point bending test with tensile stress distribution [39] (c) Fracture strength distribution [40]

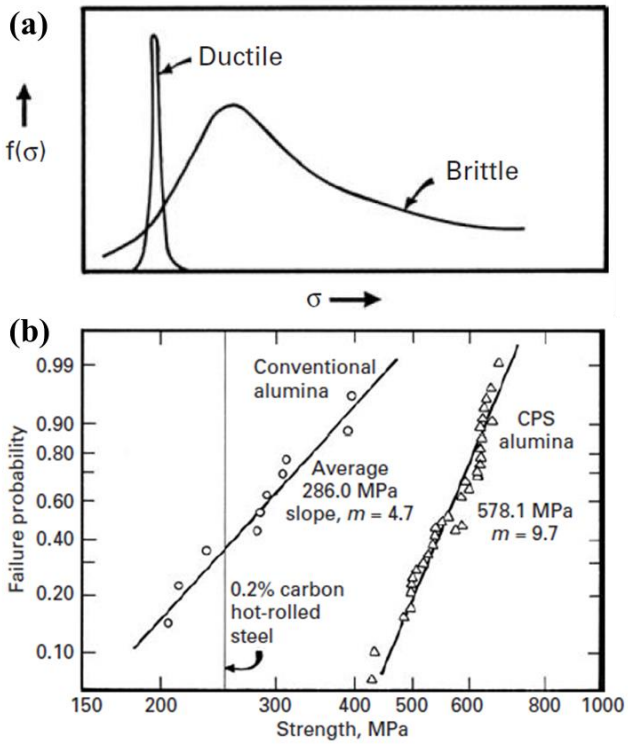

Figure 2-5. (a) Stress distribution of brittle and ductile materials (b) Weibull plot for various materials [42]

2.2. Encapsulation for flexible solar cell

2.2.1. Flexible encapsulation

The inorganic based devices have high efficiency and stability, however, the disadvantage is poor flexibility. To enhance the flexibility, the inorganic constituent layers are substituted to organic materials. The flexibility can be improved by organic substrate and layers, however, lifetime is reduced in ambient condition. The organic materials and metal electrode are highly sensitive to water vapor and oxygen, which causes degradation in the air. Especially, water vapor is strongly destructive compared to oxygen at room temperature. During device fabrication, particles are also deposited with metal cathode, resulting in pinhole formation. Water vapor size is about 3Å [43, 44] and pinhole is sufficient to be a diffusion path for water vapor, thus water vapor diffuses through the pinholes and reacts with the cathode. As a result of reaction, hydrogen gas is generated and bubbles are formed. The water vapor quickly diffuses through bubbles and devices deteriorates [45, 46]. Therefore, it is essential to introduce a technique called by encapsulation to prevent exposure to water vapor.

The conventional encapsulation method uses glass and epoxy as a top and side encapsulation respectively. This method can be used only conventional devices which consists of organic layers, metal cathode and glass substrate. The conventional devices do not require bottom encapsulation because glass substrate act as an encapsulation as well as substrate. Also, the side epoxy seal has poor barrier performance and device deteriorates from the edge due to water vapor side diffusion. This conventional encapsulation techniques have problems to apply flexible device owing to the rigidity of the substrate and barrier lid. Since the flexible devices use the organic substrate for flexibility, bottom encapsulation is also required due to poor barrier performance of substrate. Recently, flexible encapsulation techniques have been widely reported, including coated flexible substrate and thin film encapsulation.

The thin film encapsulation (TFE) techniques are classified with direct TFE and laminated TFE. The direct TFE is a method of deposition thin film directly on device without side seal epoxy. The advantages of the direct TFE are a thinner and lighter form factor and high flexibility. However, the direct process must be compatible with devices, i.e., the process must be performed at low temperature and enough high vacuum condition. The laminated TFE is a method of deposition thin film on plastic substrate (TFE substrate) and attaching it to the device using epoxy resin. Since this method uses carrier film (i.e. substrate), it is less sensitive to process condition. However, epoxy resins with low water vapor permeability become rigid after curing, thus epoxy resin breaks when deformed. The mechanical reliability is a big issue for laminated TFE [47, 48].

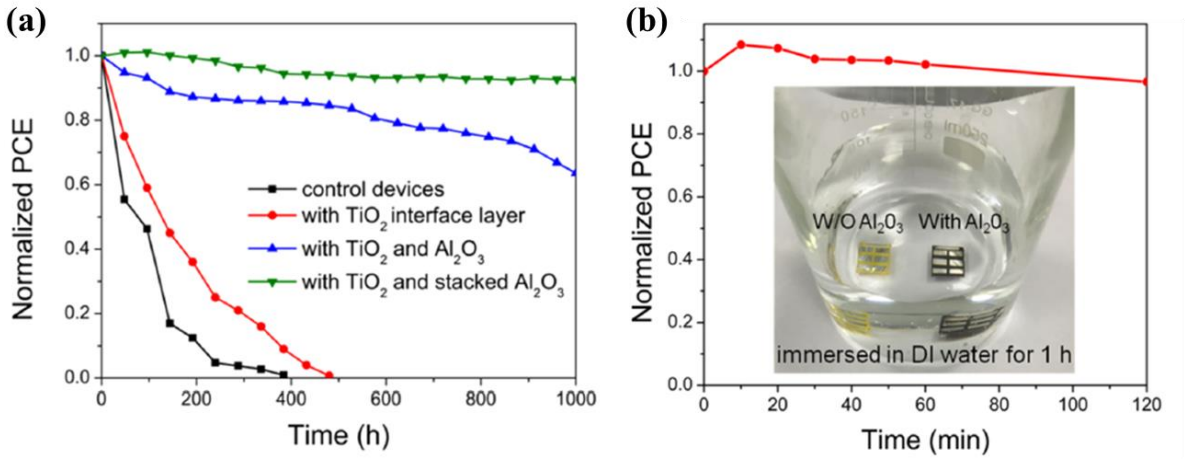

Figure 2-6. Encapsulation effect (a) Normalized PCE in an ambient condition (b) Normalized PCE of the Al_2O_3-deposited devices immersed in water. The inset photograph shows the devices without Al_2O_3 (left) and with Al_2O_3 (right) [49].

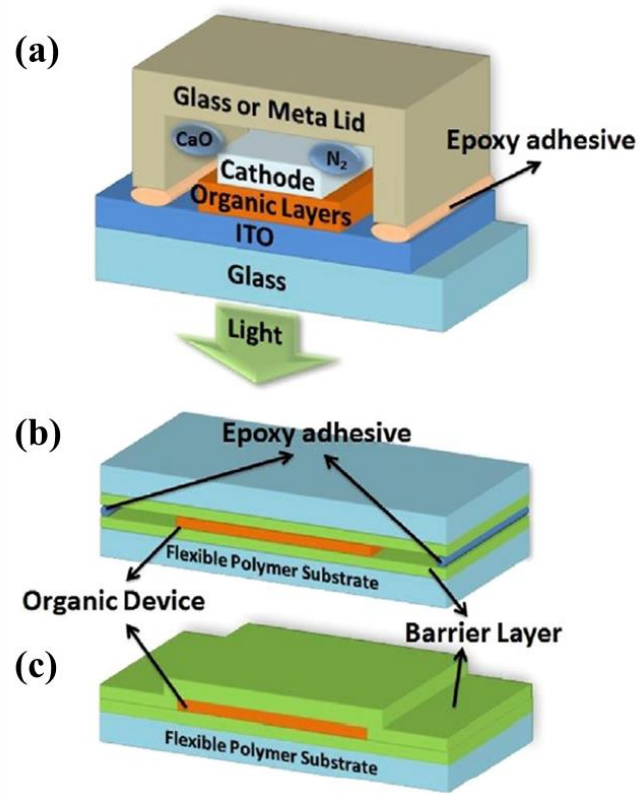

Figure 2-7. Encapsulation methods (a) Conventional glass encapsulation

(b) Laminated TFE (c) Direct TFE [48]

2.2.2. Water vapor transmission rate (WVTR)

The WVTR is representative value of barrier film performance and it means that diffusion rate of water vapor through materials. The methods of WVTR measurement can be broadly classified into three methods, i.e., MOCON, optical Ca test and electrical Ca test. The commonly used tool for measuring WVTR are instruments made for food packaging by MOCON, Inc. The water vapor is continuously supplied to one side, and after passing through film, the amount of water vapor is detected by the sensor on the other side. As a commercialized instrument, it is a most reliable methods for measuring the water vapor permeability, however, detection limit is approximately 0.005 g/m^2day for water vapor [50].

The optical Ca test and electrical Ca test are used Ca layers for measuring water vapor permeability. The Ca is very sensitive material to water vapor, when water vapor passes the barrier film, it reacts with Ca converting Ca to $Ca(OH)_2$ [26]. The chemical pathways for calcium corrosion have several potential pathways.

$$Ca + 1/2\ O_2 \rightarrow CaO \qquad n = 1/2$$

$$Ca + H_2O\ (g) \rightarrow CaO + H_2 \qquad n = 1$$

$$CaO + H_2O\ (g) \rightarrow Ca(OH)_2 \qquad n = 1$$

$$Ca + 2H_2O\ (g) \rightarrow Ca(OH)_2 + H_2 \qquad n = 2$$

Where n is the reaction ratio of calcium to permeate [51]. After oxidization, Ca become transparent and electrical resistance increases. Using those optical and electrical properties, we can measure the water vapor permeability [52, 53]. The optical calcium test tracks optical transmission changes of calcium layer resulting from the reaction of calcium with water vapor. After the calcium layer is deposited on glass, the barrier film is attached with epoxy. The optical calcium kit and experiments are shown in Figure 2-8(a) [27]. The electrical calcium test measures the electrical resistance changes of calcium layer. The metal electrode and calcium layer are deposited sequentially on glass substrate. After then, barrier film is attached to calcium deposited glass using epoxy and there should be a gas volume between the calcium and the barrier film. When there is no gas volume in calcium kit, calcium degrades inhomogeneously (defect dominant mechanism). Meanwhile, water vapor passing through barrier film disperses in the gas volume, resulting in homogeneous calcium degradation (Figure 2-9). For the electrical calcium test, homogeneous degradation of calcium is assumed, thus gas volume is required in calcium kit [54].

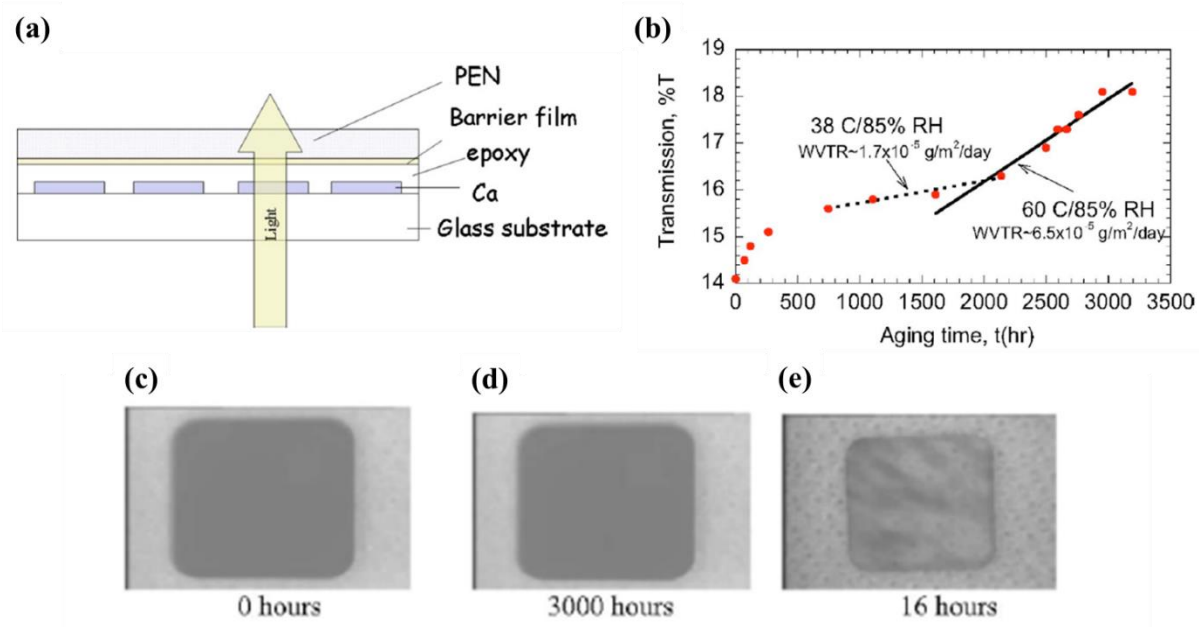

Figure 2-8. Optical Ca test (a) Ca kit for optical test (b) Optical transmission of Ca film (c) Optical image of Ca before aging (d) ALD Al_2O_3 encapsulated Ca after 3000 hours in ambient condition (e) Plastic lid encapsulated Ca after 16 hours in ambient condition [27]

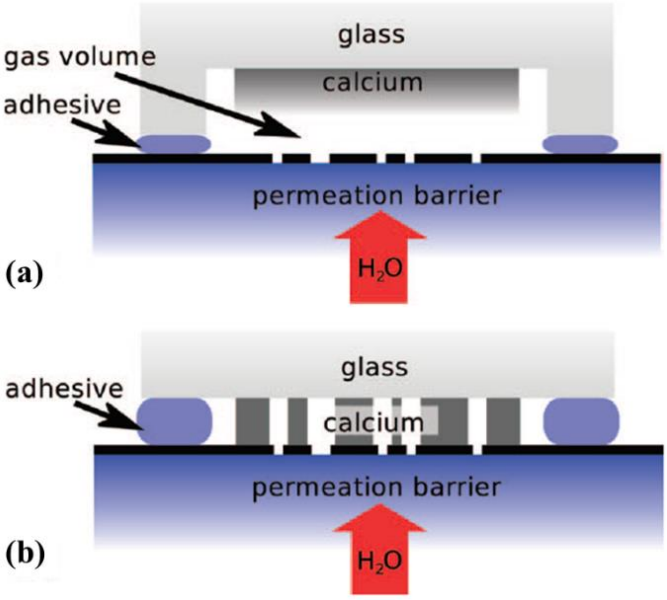

Figure 2-9. Electrical Ca test kit (a) Integral set up with gas volume (b) Localized set up without gas volume [54]

The typical WVTR graph is schematically shown in Figure 2-10(b). At initial region called by lag region, conductance change is negligible because water vapor does not pass through barrier film. The transient period is region where a small amount of water vapor diffuses and reacts with calcium layer. At last, a certain amount of water vapor is continuously supplied to calcium, thus conductance decreases linearly. This region is called by steady-state region, and we can calculate the WVTR using steady-state slope.

$$R_w = WVTR \cdot A_w \tag{6}$$

Where R_w and A_w are the transmission rate of water vapor through the barrier film and window area, respectively. The R_w can be calculated by the mass consumption rate of calcium (R_{Ca}).

$$R_{Ca} = R_w \left(\frac{M_{Ca}}{M_{H2O}}\right)\frac{1}{n} \tag{7}$$

M_{Ca} = 40.078 g/mol is the atomic mass of calcium and M_w = 18.015 g/mol is the molecular mass of water.

$$R_{Ca} = A_{Ca}\delta\frac{dh}{dt} \tag{8}$$

Where δ is the density of calcium (=1.55 g/cm^3), h is the calcium thickness and A_{Ca} is calcium area. Combining Equation. 6~8 deducts WVTR equation. (Equation. 9)

$$WVTR = n\delta\left(\frac{A_{Ca}}{A_w}\right)\left(\frac{M_{Ca}}{M_{H2O}}\right)\left(\frac{dh}{dt}\right) \tag{9}$$

$$R = \frac{\rho_{Ca} l}{wh} \tag{10}$$

Where R, ρ_{Ca}, l, w are the electrical resistance, resistivity of calcium (= 1.34X10^{-4} Ω·cm) [53, 55], length of calcium and width of calcium, respectively. Combining Equation. 9 and 10 yields WVTR

equation for the electrical resistance. (Equation. 11)

$$WVTR = n\delta\rho_{Ca}\left(\frac{l}{w}\right)\left(\frac{A_{Ca}}{A_w}\right)\left(\frac{M_{Ca}}{M_{H2O}}\right)\left(\frac{d\left(\frac{1}{R}\right)}{dt}\right) \quad (11)$$

Through the electrical calcium test, we can measure the conductance slope as time and WVTR is calculated by Equation 11 [51].

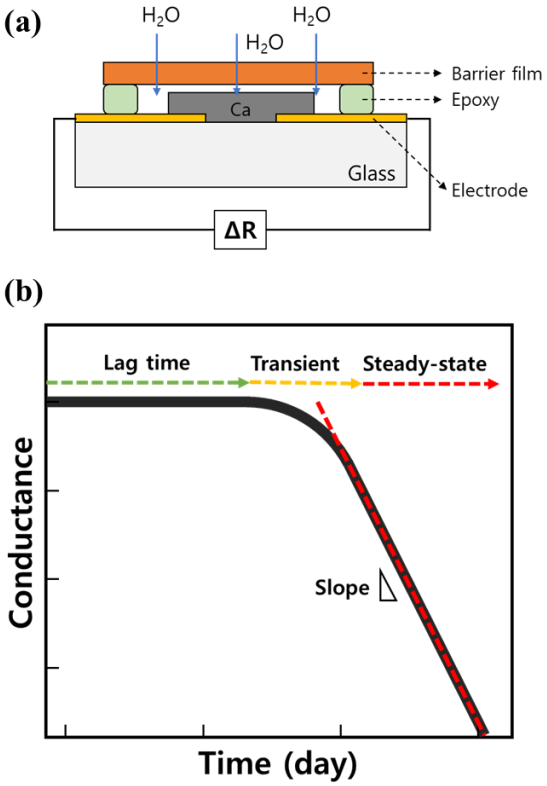

Figure 2-10. (a) Side view schematic of electrical Ca kit (b) Typical conductance-time graph for WVTR measurement

Depending on devices, required WVTR performance is different. The LCDs and TFTs composed mostly of inorganic materials require 10^{0}~10^{-4} g/m^{2}day WVTR. Meanwhile, OLEDs require below 10^{-5} g/m^{2}day WVTR [56, 57] because most of the constituent layers are organic materials which are susceptible to water vapor. The material selection is very important to reach a low-WVTR [58, 59].

The water vapor quickly passes through organic material due to internal free volume and the WVTR value of organic film is ~10^{0} g/m^{2}day. In case of inorganic materials, the WVTR is determined by nano- and macro-defects inside material. The crystallin materials have grain boundary which is the interface between two grains and atomic. The grain has less resistance to water vapor permeation compared to grain. As mentioned earlier, water vapor size is about 3Å, thus nano sized defect can act as a diffusion path of water vapor. The amorphous structure is that lack the long-range order that is characteristic of crystal, i.e., it is a randomly arranged structure with some short-range order and does not have the grain boundary like polycrystalline. In case of the high-density amorphous materials, the diffusion path can be minimized because the range of atomic length is 0.2 to 0.3 nm [43].

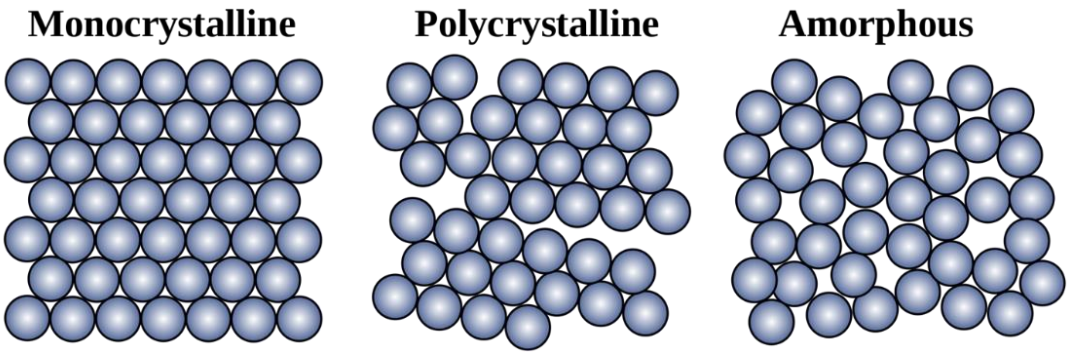

Figure 2-11. Solid structure. Copy right. WIKIPEDIA

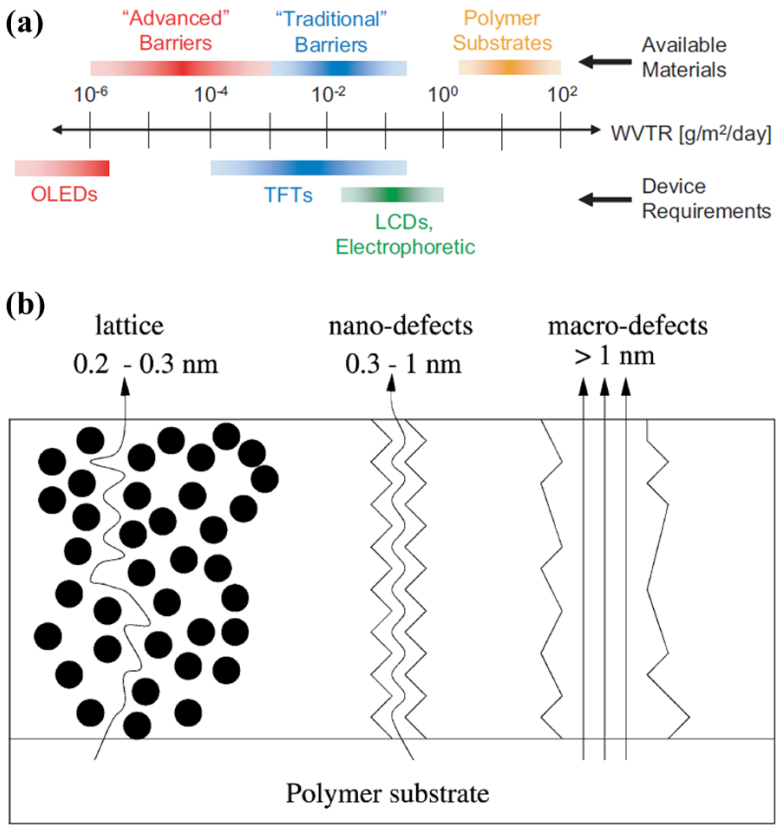

Figure 2-12. (a) WVTR for device requirements and available materials [57] (b) A schematic of proposed water vapor diffusion paths [44]

2.2.3. Griffith theory

The measured strength of bulk ceramic is ~10 times lower than theoretical value because the material has defects that act as stress concentrator, resulting in catastrophic failure [60]. Therefore, fracture strength is sensitive to surface and inside defects of materials. In macroscopic brittle materials, the fracture strength (σ_f) can be explained Equation. 12.

$$\sigma_f = \frac{K_c}{\sqrt{\pi a}} \tag{12}$$

$$\sigma_f \propto \left(\frac{1}{t}\right)^{\frac{1}{m}} \tag{13}$$

Where K_c and a is the fracture toughness and intrinsic flaw size, respectively. Equation. 12 shows that the fracture strength of brittle materials is inversely proportional to the square root of the intrinsic flaw size, which act as a stress concentrator for crack initiation and reduce fracture strength. In bulk scale materials, the crack propagates at a low applied stress due to the relatively high probability of including pre-existing defects of various sizes. In small-scale materials, the relatively low probability of including pre-existing defects leads to relatively high fracture strength.

The fracture strength can be explained by Weibull statistics. (Equation. 13) Where t and m are thickness of material and Weibull modulus, respectively. Equation. 13 means that smaller is strength. In the nano-scale material, fracture strength increases as size decreases up to critical thickness. The size effect has already been proved theoretically and experimentally. Below a critical thickness, fracture strength does not increase and saturates, it means that the material reaches theoretical strength. The reasonable range of theoretical strength is between E/2π and E/30 [61, 62]. The critical thickness (h*) can be calculated by Equation. 14.

$$h^* = \alpha^2 \frac{\gamma E}{\sigma_{th}} \tag{14}$$

Where γ, E and σ_{th} are surface energy, elastic modulus and theoretical strength, respectively. When the material size is larger than critical thickness, the fracture strength is sensitive to size and pre-existing defects. However, when the material size is smaller than critical thickness, the material becomes insensitive to pre-existing defects and fracture strength reaches the theoretical strength [63].

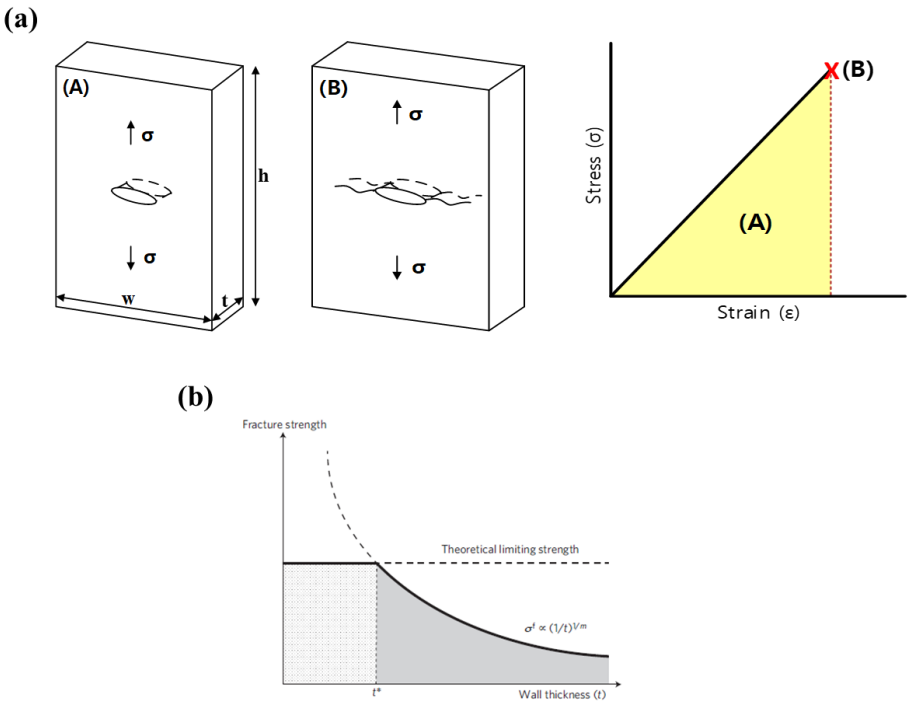

Figure 2-13. (a) Mechanical behavior of brittle solids. Before fracture, solid has elastically stored energy inside (A) and crack propagates when the released elastically stored energy is at least equal to the energy required to generate new crack surface. (B) (b) Size effect of brittle solid and theoretical strength [62]

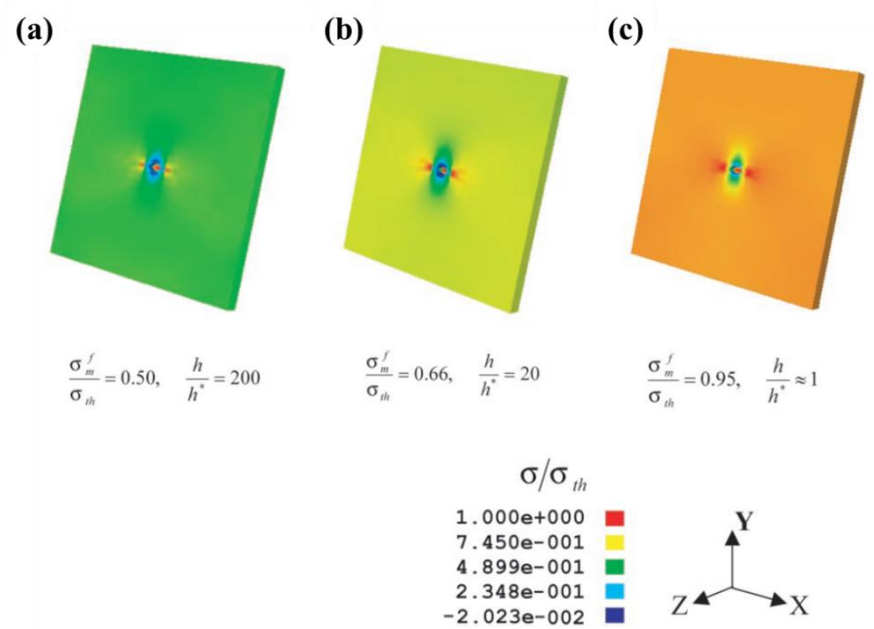

Figure 2-14. FEM simulation results of stress distribution (a) Large thickness, the stress concentrates on the flaw (b) Stress concentration at flaw is reduced relatively. (c) The critical thickness, the stress distributes whole sample and strength reaches the theoretical strength [63].

2.2.4. Atomic layer deposition (ALD)

The ALD process is thin film deposition technique that is based on the sequential use of a gas chemical process. The precursor reacts with oxidant gas and the film is deposited with atomic-scale layer. When the thin film is deposited by ALD, the high-density film can grow uniformly due to self-limiting reaction and film can be deposited not only on the top of the substrate, but also on the edges owing to good stepcoverage [64, 65]. The pinhole-free deposition is also advantage of ALD. The ALD process consists of 4 steps. 1) The precursor reacts with hydroxyl (OH) groups attached to the substrate. After reaction, residual precursors can no longer react. 2) Byproducts and residual gas are removed by N_2 or Ar gas and this step is called by purging. 3) The oxidant gas is injected in the main chamber and atomic-oxide layer is generated on the substrate. After reaction, residual oxidant gas also can no longer react. 4) The purge process is repeated. These complete 4 steps are expressed as 1 cycle and film thickness increases as the number of cycle increases. The required thickness of film can be deposited by controlling the number of cycles [66]. The ALD can be classified as thermal ALD and plasma-enhanced ALD (PEALD) according to the oxidant gas.

Thermal ALD uses water vapor as an oxidant and the high-density film can be deposited at high growth temperature. Based on previous research, hydrogen concentration increases and film density is reduced in the Al_2O_3 ALD film because rate of water vapor desorption is slow at low process temperature. To prevent this problem, very long water vapor purge time is required and total process time also increases [67, 68].

PEALD uses oxygen plasma as an oxidant. Since oxygen plasma has high reactivity with precursor, the growth rate is faster than that of thermal ALD, resulting in a relatively short process time. Also, high quality film can be grown on the substrate at low temperature. The low temperature process is very important for encapsulation because plastic substrate and organic layers are deformed at high temperature [68-70].

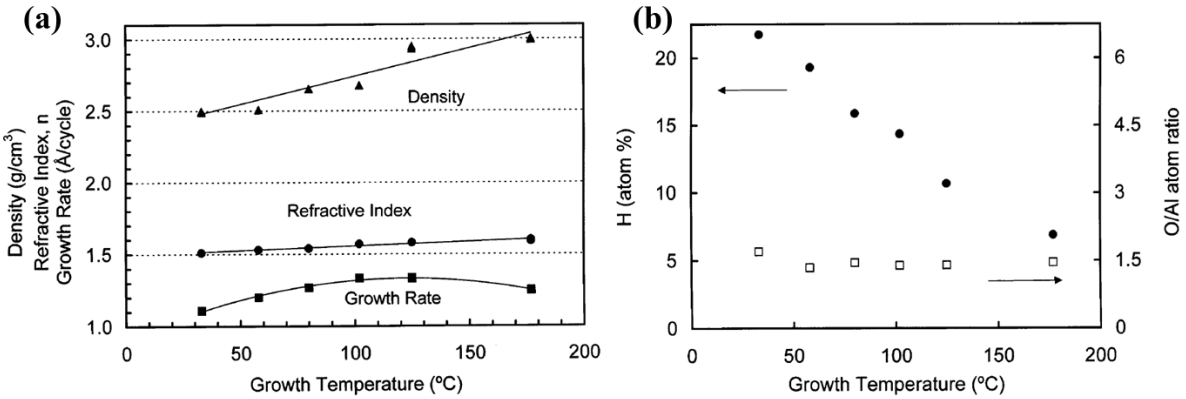

Figure 2-15. (a) Density, refractive index and growth rate of ALD Al_2O_3 depending on growth temperature (b) Hydrogen concentration depending on growth temperature [67]

	growth temperature (°C)					
	177	125	102	80	58	33
TMA exposure time (s)	1	1	1	1	1	1
purge time (s)	5	5	5	5	10	20
water exposure time (s)	1	2	2	2	2	2
purge time (s)	5	10	20	20	30	180
mass gain/cycle (ng/cm^2)	38	39	36	34	30	28

Table 2-1. Process condition of thermal ALD depending on growth temperature [67]

2.2.5. Amorphous Al_2O_3 by ALD

The amorphous Al_2O_3 films are used for various applications such as gas- and moisture-diffusion barriers. Especially, Al_2O_3 film deposited by ALD have good step coverage, high density and low surface roughness. The high-density Al_2O_3 film can be grown by thermal ALD and PEALD. The $Al(CH_3)_3$ [tri-methylaluminum (TMA)] is precursor and H_2O, oxygen plasma are used as an oxidant. The TMA and water vapor produce amorphous Al_2O_3 according to the two reactions.

$$AlOH^* + Al(CH_3)_3\ (g) \rightarrow AlOAl(CH_3)_2^* + CH_4\ (g)$$

$$AlCH_3^* + H_2O\ (g) \rightarrow AlOH^* + CH_4\ (g)$$

Where the asterisks represent surface species. These two reactions are expressed as a cycle and thickness of film increases linearly [67, 71]. By PEALD process, the TMA and oxygen plasma yield amorphous Al_2O_3 according to the following two reactions [72].

$$AlOH^* + Al(CH_3)_3\ (g) \rightarrow AlOAl(CH_3)_2^* + CH_4\ (g)$$

$$AlCH_3^* + 4O\ (g) \rightarrow AlOH^* + CO_2\ (g) + H_2O\ (g)$$

The amorphous Al_2O_3 film has several advantages for use as an encapsulation material. The encapsulation material is required >90% optical transmittance for high efficiency devices. The ALD Al_2O_3 layer has a high transmittance greater than 95% in previous research [73]. Also, when Al_2O_3 film is deposited on plastic substrate, transmittance is improved due to anti-reflectance effect [74]. Comparing between bare plastic substrate and Al_2O_3 coated plastic substrate, transmittance of Al_2O_3 coated substrate is greater than that of bare substrate (Figure 2-17).

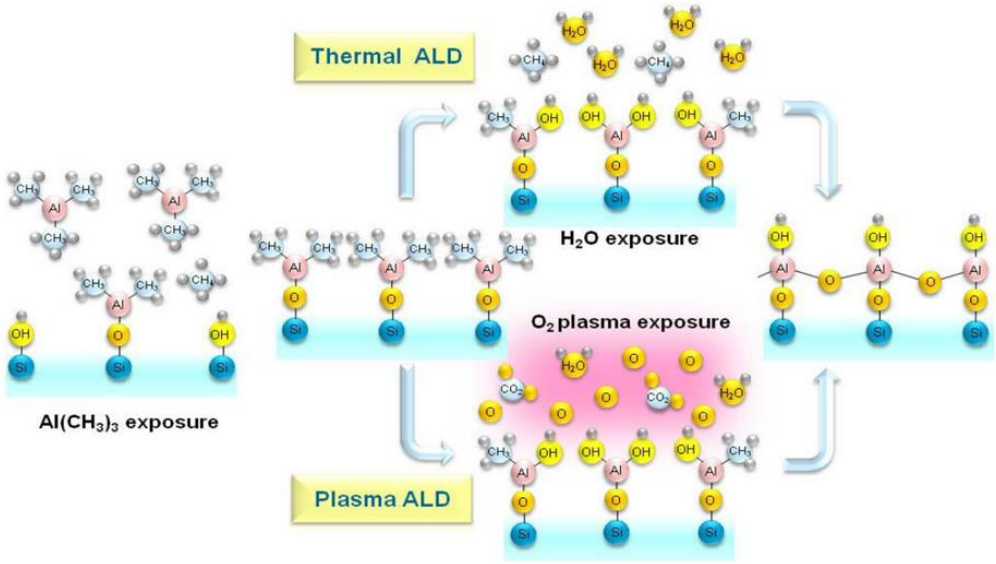

Figure 2-16. Process of thermal ALD and PEALD for Al_2O_3 [75]

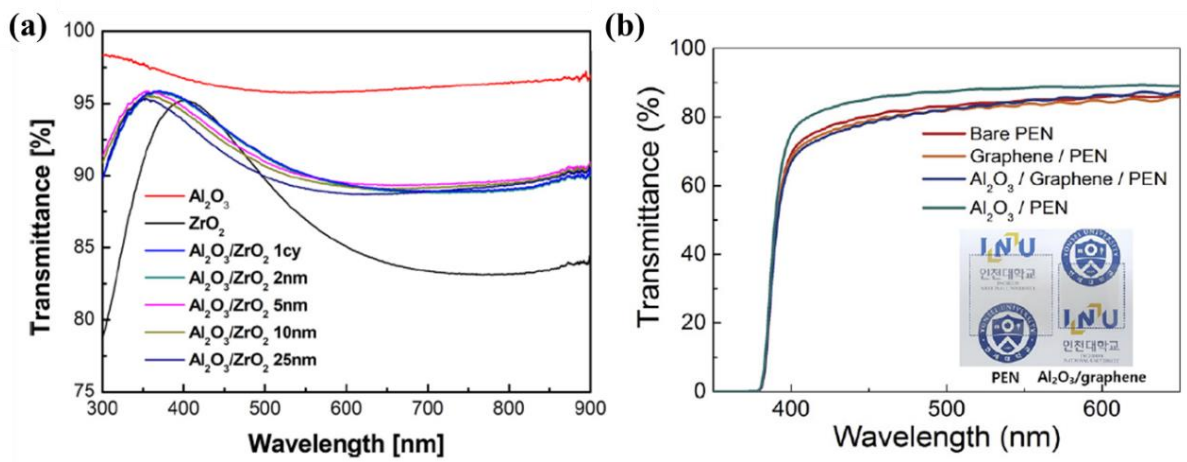

Figure 2-17. (a) Optical transmittance of single layers and multilayers [73] (b) Optical transmittance of coated plastic substrates [74]

As shown in Table 2-2, WVTR of the amorphous Al_2O_3 films by ALD shows very low water vapor permeability (10^{-4}~10^{-5} g/m^{2}day). Those results mean that even a single Al_2O_3 film can reach a sufficiently low-WVTR value. In Table 2-2, the critical bending radius represents bending radius when the crack propagates. In most case of previous studies, cyclic bending tests are performed and WVTR is measured after bending to analyze the flexibility. This method has limitations in evaluating accurate flexibility and the mechanism analysis for the degradation of WVTR value after cyclic bending is still insufficient, except for crack formation.

Kwon et al. [43] reported flexible thin film encapsulation using inorganic/organic hybrid material. In this study, WVTR of Al_2O_3 single layer is degraded after bending at 1.67 cm bending radius without crack formation and cracks propagate after bending at 1 cm bending radius. Based on changes in WVTR, nano-sized cracks that cannot be seen in SEM can be formed by applied stress and water vapor can easily diffuse through nano-sized cracks, i.e., WVTR is affected by invisible nano-sized cracks in small strain.

Reference	Method	Temperature (℃)	Thickness (nm)	WVTR (g/m^{2}day)	Critical bending radius
[22]	ALD	80	20	7.8 X 10^{-4}	5.3 mm
[23]	PEALD	100	50	3.75 X 10^{-4}	-
[26]	ALD	80	100	2 X 10^{-5}	-
[43]	ALD	70	60	8.065 X 10^{-5}	10 mm
[74]	ALD	100	50	3.07 X 10^{-4}	7.5 mm
[76]	ALD	70	30	8.53 X 10^{-4}	-
[77]	ALD	80	130	9.9 X 10^{-5}	-
[78]	PEALD	100	50	4.16 X 10^{-4}	-

Table 2-2. WVTR value of ALD-Al_2O_3 thin films

The measurement of mechanical properties is important for analyzing the flexibility. In previous research, mechanical properties of ALD Al_2O_3 are measured by various methods. As shown in Table 2-3, elastic modulus of Al_2O_3 films is on average around 180 GPa at high growth temperature (150~300℃). However, elastic modulus decreases to 138.5 GPa when the growth temperature is 110℃. Since elastic modulus is affected by density of bonds, elastic modulus increases with increasing growth temperature [79]. At the lower temperature, hydrogen impurity concentration increases and density of film is reduced. It means that we can confirm the quality of film through mechanical properties as well as optical properties.

The elastic limit is very important value to estimate the flexibility and tensile testing is an experimental method that measures the accurate strain. Bauer et al. [80] reported that calculated tensile strength and strain of ALD Al_2O_3 through push-to-pull tensile tests of ALD coating on 3D printed polymer. Rest et al. [81] estimated the elastic limit of sputter deposited Al_2O_3 films using hardness by nanoindentation. These studies indirectly measured and analyzed the tensile properties of Al_2O_3 thin films. In most case of previous studies., studies on the tensile properties of ALD Al_2O_3 thin films are still insufficient.

Growth temperature [°C]	Pulse sequence [s]	Growth cycles	Thickness [nm]	Elastic modulus by nanoindentation [GPa]	Elastic modulus by LSAW [GPa]	Hardness [GPa]
(Si ref)	–	–	–	153.7 ± 6.4	–	10.2 ± 0.4
110	0.1-4-0.1-4	3933	288.3	138.5 ± 8.4	–	7.9 ± 0.2
150	0.1-4-0.1-4	3411	285.4	171.2 ± 11.6	–	10.0 ± 0.2
200	0.1-4-0.1-4	3120	286.7	166.6 ± 10.7	–	9.8 ± 0.3
250	0.1-4-0.1-4	3115	291.9	178.0 ± 14.4	–	11.1 ± 0.7
300	0.1-1-0.1-1	100	9.9	–	170.2 ± 2.8	13.8 ± 0.9
300	0.1-1-0.1-1	200	19.8	–	169.4 ± 1.6	13.3 ± 0.4
300	0.1-1-0.1-1	500	48.5	166.2 ± 10.3	173.1 ± 0.6	10.1 ± 0.3
300	0.1-1-0.1-1	1000	96.1	172.9 ± 9.4	174.7 ± 0.2	10.4 ± 0.4
300	0.1-1-0.1-1	3000	283.7	169.8 ± 9.8	175.0 ± 0.8	10.5 ± 0.5
300	0.1-1-0.1-1	6000	566.9	172.8 ± 10.8	176.0 ± 1.0	10.3 ± 0.6

Table 2-3. Mechanical properties of ALD-Al_2O_3 films [79]

3. Flexibility of ultra-thin silicon of flexible silicon solar cell

3.1. Introduction

Among the various types of solar cells, crystalline silicon (Si) solar cells are widely used due to their high energy-conversion efficiency and application feasibility. Recently, thin silicon solar cells with a typical wafer thickness less than 100 um, which are flexible and possess the advantages of silicon solar cells, have been developed. Thin silicon wafers are very fragile [82]; therefore, understanding the critical bending radius is important. Surface texturing of silicon wafer has been widely used to reduce reflectivity and enhance light-trapping efficiency [83, 84]. However, the surface textures in these silicon wafers act as stress concentrators for mechanical deformation, which can reduce the flexibility of thin silicon solar cells [31]. The widely used surface texturing in silicon wafers is the patterning of randomly patterned pyramids, which is accomplished by chemical etching using potassium hydroxide (KOH) solution in which the etch rates are dependent of the crystallographic orientations of silicon [18, 31]. Meanwhile, the reflectivity is reduced to approximately 15% due to pyramid surface texturing, and the flexural strength is weakened even in thick silicon wafers. On the other hand, thin single-crystalline silicon solar cells with surface texturing have been reported to demonstrate higher power conversion efficiency in a bent state and are more durable for cyclic bending [20, 85]. When a silicon wafer has a single large notch, surface texturing in a fine and periodic array enhances the flexural strength of the silicon wafer because the stress concentration at the large notch is effectively dispersed by the surface texturing [38]. The mechanical behavior of thin single-crystalline silicon wafers with surface texturing strongly depends on the shape, scale, and distribution of the textured patterns; thus, investigating the effects of surface texturing on the flexibility of thin silicon wafers are highly required.

In this study, we performed surface texturing with pyramid and dome shapes on a 50-um-thick single-crystalline silicon wafer. We carried out four-point bending tests on three samples with non-, dome-, and pyramid-textured surfaces. They showed elastic bending followed by catastrophic failures. The flexural strengths were analyzed using Weibull distribution, and the critical bending radius was measured. We found that the dome surface texturing has higher flexural strength and smaller critical bending radius than the pyramid surface texturing, whereas the light reflectance was similar to or lower than that of the pyramid-textured sample [86], suggesting that dome pyramid surface texturing is more appropriate for flexible solar cells.

3.2. Preparation of surface textured silicon

Figure 3-1 shows the fabrication processes of the textured ultra-thin silicon samples. At first, thin silicon was fabricated by wet etching. Both side-polished (100) silicon wafers with a thickness of 300 um were chemically etched in 45 wt.% KOH solution at 90 °C. The temperature of KOH solution was kept uniformly using a silicon oil bath. We obtained 50-um-thick thin silicon wafers, which refers to a planar surface or a non-textured sample. Using the thin silicon wafers, we performed surface texturing on the dome- and pyramid-textured surfaces.

To form a pyramid-textured surface, we deposited a 400-nm-thick silicon nitride layer as a protective layer at the backside of the wafers using plasma-enhanced chemical vapor deposition. After then, the wafers are immersed in 5 wt.% KOH and 20 vol.% isopropyl alcohol (IPA)-mixed solution at 70 °C for 30 min. As a result of the anisotropic etch rate of silicon in low-concentration KOH solution, randomly distributed pyramids were formed on the surface [18]. The depth of the pyramids ranged from 3 to 10 um. The silicon nitride protective layer was removed using a 25 wt.% hydrogen fluoride (HF) solution.

Figure 3-1 (b) shows the process for the dome-textured surface. SiO_2 beads with a diameter of 500 nm, which acted as a hard mask in the subsequent reactive ion etching (RIE) process, were spread on a planar surface in a packed monolayer by spin coating. This surface was etched to RIE using CF_4 gas and O_2 plasma until the SiO_2 beads were removed. Nano domes with a depth of 300 nm were patterned. Three samples are named as non-, dome-, and pyramid-textured samples.

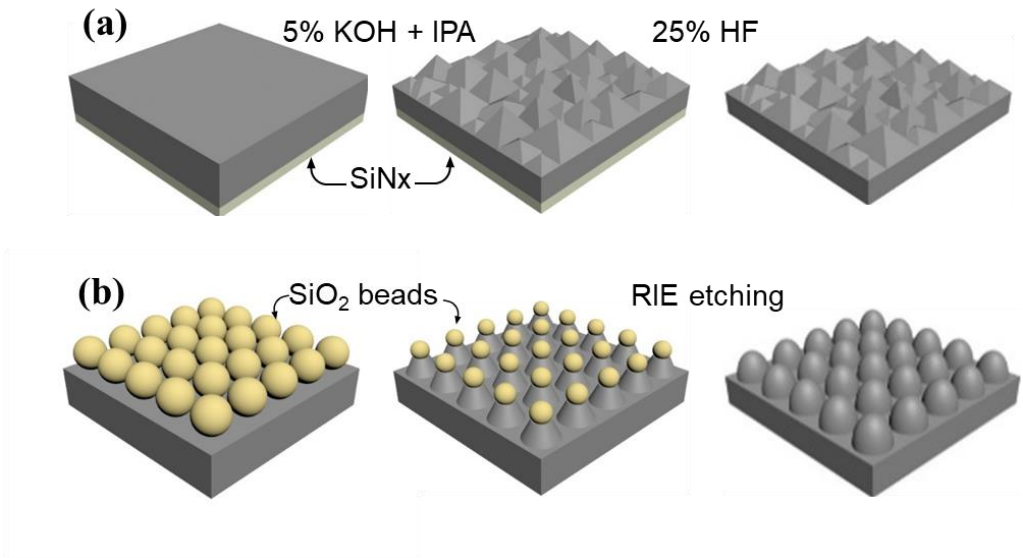

Figure 3-1. Preparation of surface textured samples (a) Pyramid- and (b) Dome-texturing

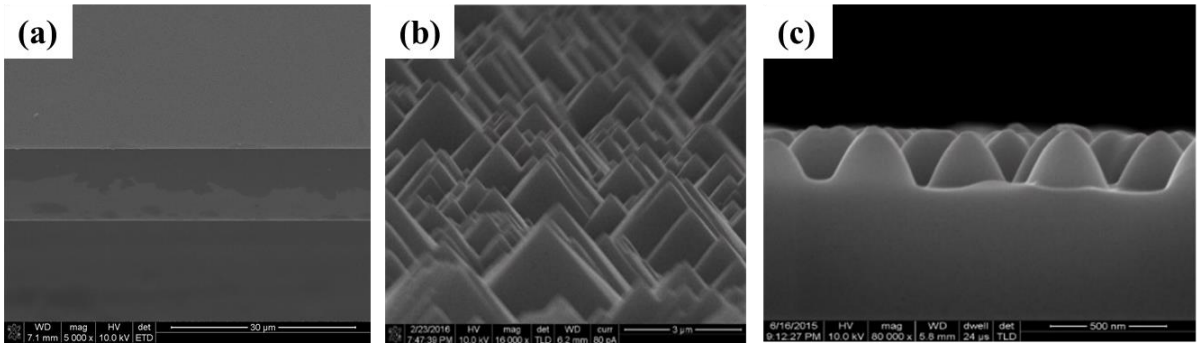

Figure 3-2. SEM images of (a) Non-, (b) Pyramid- and (c) Dome textured silicon

3.3. Flexural strength of surface textured silicon

To analyze the bending properties, 4-point bending tests are conducted. The non-, dome- and pyramid-textured samples were cut in the shape for a four-point bending test with a width of 3 mm and a length of 13 mm using laser scribing. Four-point bending tests were carried out at a loading rate of 2 um/s, and movie recording was performed using a universal testing machine (Instron 5948). Because of the catastrophic failure of the three samples, at least 30 four-point bending tests were performed for each sample [87].

Flexural strength σ_f is calculated using the following equation:

$$\sigma_f = \frac{3PL}{4bd^2}, \tag{15}$$

where P, L, b, and d are the applied force at fracture, distance between the support spans (8 mm), sample width (3 mm), and sample thickness, respectively. Flexural strength is 124 MPa (±40.5) for non-textured samples, 95 MPa (±19.8) for dome-textured samples and 82.8 MPa (±16.8) for pyramid-textured samples.

3.4. Weibull distribution

The flexural strength distribution was statistically analyzed using the Weibull distribution due to high standard deviation. Characteristic strength σ_0 which corresponds to a survival probability of 37% [38, 88], is 138.5 MPa for the non-textured samples, 103.4 MPa for the dome-textured samples, and 89.8 MPa for the pyramid-textured samples. The characteristic strength of the flexural strength was on the order of non-, dome-, and pyramid-textured silicon samples. Surface texturing forms surface notches that act as stress concentrators; thus, the flexural strengths of the dome- and pyramid-textured samples are lower than that of the non-textured sample. Pyramid texturing can likely form sharper and deeper notch than dome texturing, resulting in higher flexural strength of the dome-textured silicon sample, which will be discussed in detail later. Weibull modulus m was 3.28 for the non-textured samples, 5.0 for the dome-textured samples, and 5.21 for the pyramid-textured samples. The Weibull modulus corresponds to the magnitude of scattering in the data. A lower Weibull modulus results in wider distribution [89]. The three samples all showed elastic bending and catastrophic failure in the four-point bending tests, which means that the flexural strength depends on the highest stress

concentrator between the inner spans where identical tensile stress is applied at the surface. The thin silicon wafer with a planar surface has the lowest Weibull modulus than the two textured surfaces.

This result indicates that the flexural strength of a non-textured sample depends on the probability of containing the highest stress concentrator that is possibly generated in the thinning process by wet etching or wafer growth [7, 9, 38]. In the other two surface-textured samples, surface texturing most likely provides the highest surface concentrators. The pyramid-textured sample has a higher Weibull modulus than the dome-textured sample, which implies that irregular stress concentrators are introduced at the pyramid-textured surface.

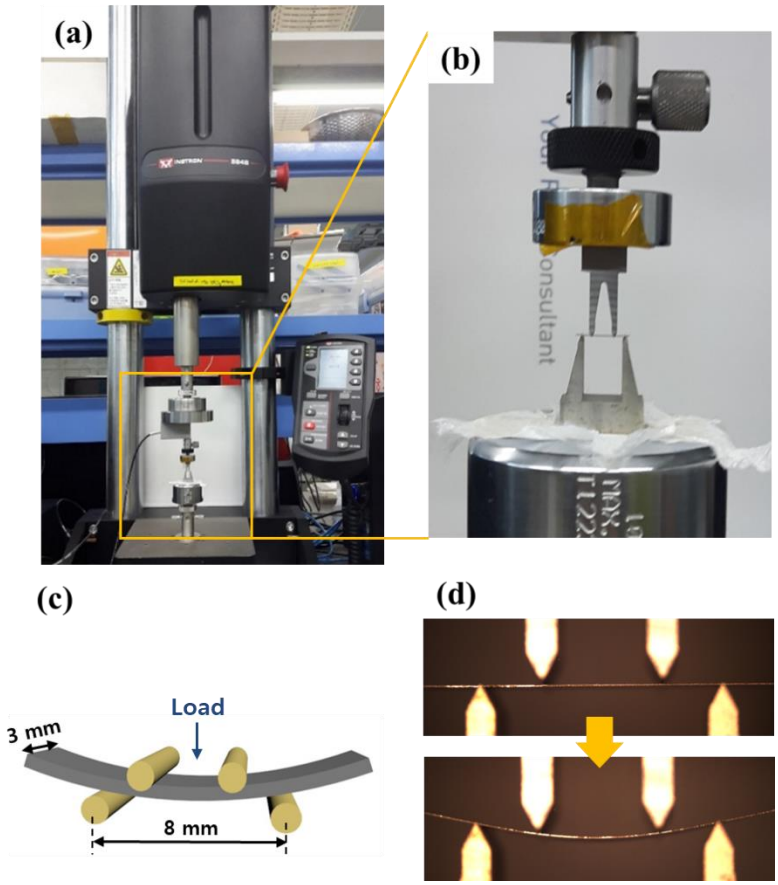

Figure 3-3. Set-up for 4-point bending test (a) Instron 5948 (b) Photograph of sample located in jig (c) Schematic of 4-point bending test (d) Optical microscope images of before/after sample deformation

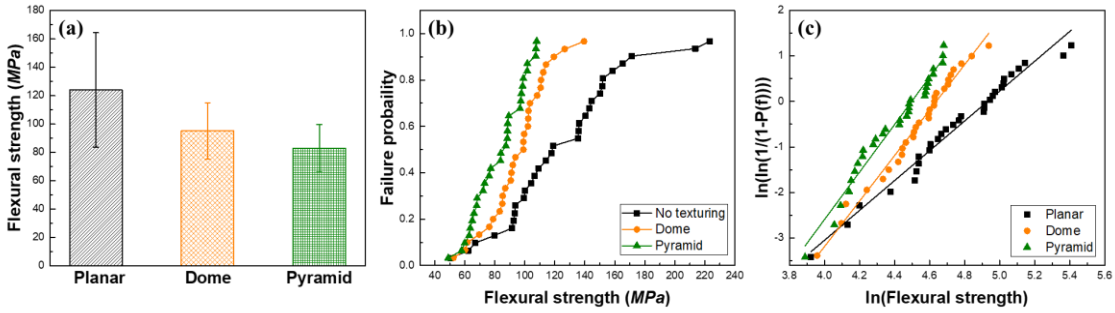

Figure 3-4. (a) Flexural strength of surface textured samples (b) Failure probability of flexural strength (c) Weibull distribution for flexural strength

3.5. Stress concentration analysis

3.5.1. Theoretical analysis

Figure 3-5 (b) and (c) shows typical cross-sectional SEM images of a fracture surface for the dome- and pyramid-textured samples. The dome texturing formed V-shape notches with notch angle α of 75° and tip radius r of 68 nm. SiO_2 beads with hard mask RIE for dome texturing were spun-coated in the form of closed-packed monolayer in most areas where periodic domes were formed. Some silicon surface areas, which were approximately 3% of the total surface area that were not coated by SiO_2 beads, were subjected to RIE, and flat valleys were formed on the dome-textured silicon sample, which had no sharp notches that induced stress concentration. In the pyramid-textured samples, V-shaped notches with α of 70.5° and r of 28 nm were formed. The size of the pyramids was irregular, ranging from a pyramid depth of 3 to 10 um, and the tip radius was not dependent on the pyramid size. The schematic of the rectangular parallelepiped with a single notch shown in Figure 3-5 (a) describes stress-concentration factor K as

$$K=\sigma_{max} / \sigma_{nom}, \tag{16}$$

where σ_{max} is the maximum stress at the notch tip and σ_{nom} is the nominal stress far from the notch [38], which is expressed as $\sigma_{nom} = 6M/wt^2$, where M is the bending moment, w is the width, and t is the thickness of sample [90]. The measured stress-concentration factors of the dome- and pyramid-textured samples, which were calculated using the ratio of characteristic strength σ_0 to that of the non-textured sample, were 1.34 and 1.54, respectively.

In case of the single notch, stress concentration factor is affected by geometrical factors : notch angle, dept of notch and tip radius of notch. When notch angle α is smaller than 90°, the stress-concentration factors of the U- and V- shaped notches are identical, which means that the difference in $\alpha = 75°$ for the dome-textured sample and $\alpha = 70.5°$ for the pyramid-textured samples did not influence the stress concentration at the tips of the surface textures. The stress-concentration factor at the tip of a single U-notch is expressed following equation which for $2.0 \leq h/r \leq 20.0$ [90].

$$K = C_1 + C_2\left(\frac{h}{t}\right) + C_3\left(\frac{h}{t}\right)^2 + C_4\left(\frac{h}{t}\right)^3 \tag{17}$$

Where *h* indicates the depth of notch as shown in Figure 3-5 (a). The *h* of dome and pyramid is measured by SEM (Figure 3-6).

$$C_1 = 0.953 + 2.136\sqrt{\frac{h}{r}} - 0.005\left(\frac{h}{r}\right) \quad (18)$$

$$C_2 = -3.255 - 6.281\sqrt{\frac{h}{r}} + 0.068\left(\frac{h}{r}\right) \quad (19)$$

$$C_3 = 8.203 + 6.893\sqrt{\frac{h}{r}} + 0.064\left(\frac{h}{r}\right) \quad (20)$$

$$C_4 = -4.851 - 2.793\sqrt{\frac{h}{r}} - 0.128\left(\frac{h}{r}\right) \quad (21)$$

The stress-concentration factor at the single U-notch tip with a notch depth of 300 nm and a tip radius of 68 nm, which corresponded to dome texturing, was 5.54 and we could estimate that stress-concentration factor of the pyramid texturing is greater than 5.54 because it had higher *h*/*r* than the dome texturing. However, we did not quantitatively present this because the equation of the stress-concentration factor is valid only up to *h*/*r* = 20 (a notch depth of 10 um and a tip radius of 28 nm corresponding to pyramid texturing). These values are much greater than the measured 1.34 for dome texturing and 1.54 for pyramid texturing, which can be possibly attributed to the dispersion of stress concentration due to surface texturing. According to previous reports, fine and periodic array of notches more effectively disperse the stress concentration at the highest stress concentrator, resulting in a low stress-concentration factor [91].

3.5.2. Stress distribution analysis by FEA simulation

The stress and strain distributions were analyzed by finite element analysis (FEA). Abaqus 6.12 and Abaqus CAE were used for the FEA simulations and creation of input files, respectively. A two-dimensional deformable shell model was applied, and sample geometries in FEA were designed based on typical cross-sectional scanning electron microscopy (SEM) images of the experimental samples. Young's modulus of 169 GPa and Poisson's ratio of 0.27 were set as the mechanical properties of the silicon wafer [8, 92, 93]. Figure 3-7 shows that the stress-concentration factor calculated using the FEA results for dome texturing is 3.15 and that for pyramid texturing is 4.50. In the FEA simulations, the highest stress concentration was attained at the location with the greatest *h*/*r* value for both dome and pyramid texturing. The distributions of the von Mises stress show that the stress concentration at the tips of the surface patterns effectively dispersed, depending on the geometries of the neighboring

notches, which resulted in lower stress-concentration factors, namely, 3.15 for dome texturing and 4.50 for pyramid texturing, than the theoretical values of a single notch. However, these values were higher than the measured ones, namely, 1.34 for dome texturing and 1.54 for pyramid texturing.

Two-dimensional models were used in the FEA simulations, indicating linear notches through the thickness direction in the three-dimensional samples. In the surface-textured samples, domes and pyramids were also distributed along the thickness direction; thus, dispersion of the stress concentration was also effective along the thickness direction. The measured stress-concentration factors of 1.34 for dome texturing and 1.54 for pyramid texturing, which were much lower than the value of the single notch, could be most likely attributed to the effective dispersion of stress concentration in the fine and periodic array of dome patterns and irregular distribution of pyramid patterns.

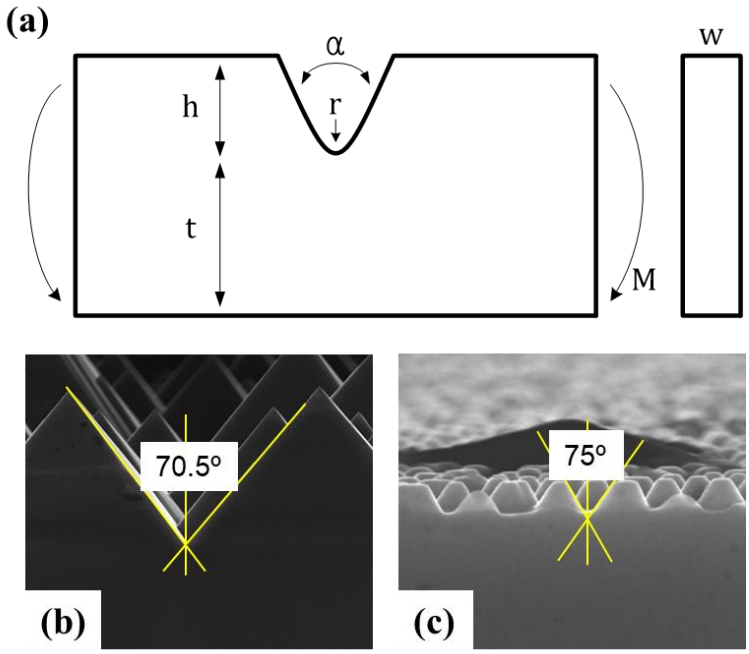

Figure 3-5. (a) Schematic of single notch geometry (b), (c) Notch angle of pyramid and dome

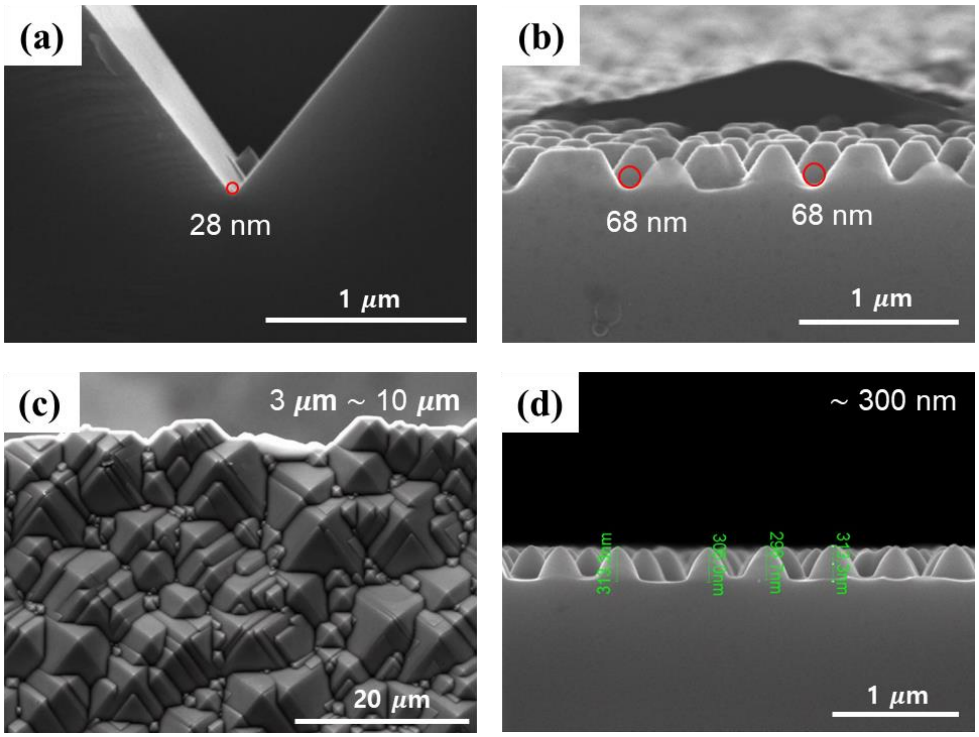

Figure 3-6. (a), (b) Notch tip radius of pyramid and dome (c), (d) Notch depth of pyramid and dome

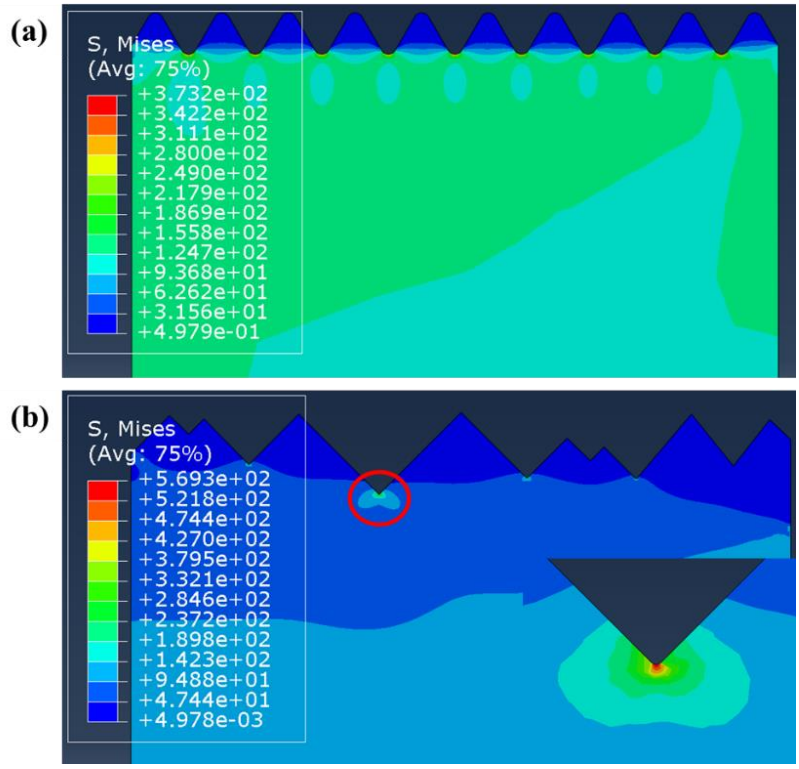

Figure 3-7. FEM analysis of von Mises stress distribution (a) Dome and (b) Pyramid texturing

3.6. Critical bending radius of textured silicon

Figure 3-8 shows the critical bending radius of the three samples measured immediately before fracture in the four-point bending test. The critical bending radius was 37.1 (±11.5) mm for the non-textured samples, 46.8 (±14.2) mm for the dome-textured samples, and 59.3 (±17.5) mm for the pyramid-textured samples. The critical bending radius for the dome-textured sample was 26.1% greater than that of the non-textured sample and 26.7% smaller than that of the pyramid-textured sample. The dome-textured sample was more flexible than the pyramid-textured sample. In a previous study, the reflectance was found to range from 35% to 40% for the non-textured surface, from 10% to 15% for the pyramid-textured surface, and from 4% to 15% for the dome-textured surface. In the wavelength range between 700 nm and 900 nm, the reflectance of the dome-textured surface was lower than that of the pyramid-textured surface [86]. In terms of the light-trapping effect and mechanical flexibility, dome texturing exhibited better performance than pyramid texturing.

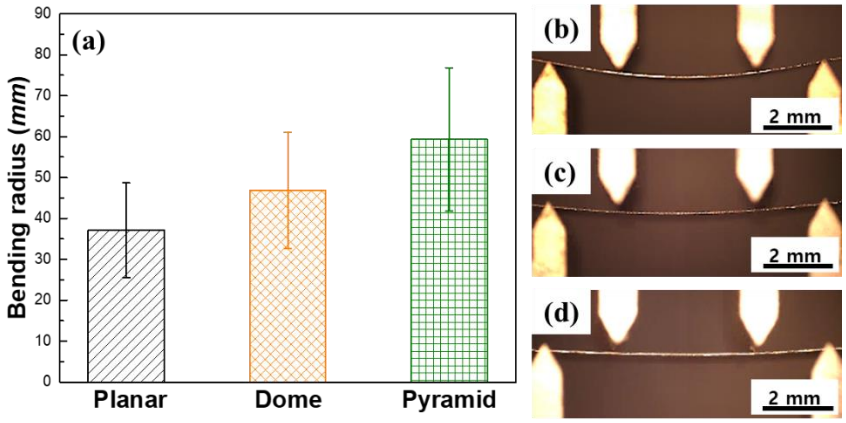

Figure 3-8. (a) Critical bending radius and typical optical microscope images immediately before fracture (b) Non- (c) Dome-, and (d) Pyramid-textured silicon

3.7. Conclusion

In this research, we analyzed the surface texturing effects on mechanical properties of silicon substrate used in solar cell. The flexural strength and critical bending radius were measured by 4-point bending radius. These results were statistically analyzed by Weibull distribution. By the Weibull analysis, the characteristic strength was 138.5 MPa for the non-textured sample, 103.4 MPa for the dome-textured sample, and 89.8 MPa for the pyramid-textured sample. Weibull modulus *m* is 3.28 for the non-textured samples, 5.0 for the dome-textured samples, and 5.21 for the pyramid-textured samples. These results were affected by the stress concentration of the geometries of the surface textures.

Based on characteristic strength, stress concentration factor for dome-textured samples was 1.34 and that for pyramid-textured samples is 1.54. With respect to the single-notch concept, calculated stress concentration factor for dome-textured samples was 5.54, however, value of pyramid-textured samples was not calculated owing to high h/r ratio. As results of 2D FEA simulation by fracture SEM images, stress concentration factor of dome- and pyramid-textured samples are 3.01 and 4.59, respectively. The pyramids formed deeper and sharper notches than the domes, which induced higher stress concentration and resulted in lower flexural strength.

At last, we analyzed the critical bending radius of surface textured silicon through image just before fracture. The critical bending radius of the non-, dome-, and pyramid-textured samples were 37.1, 46.8, and 59.3 mm, respectively. The dome-textured silicon is more flexible than pyramid-textured silicon.

4. Flexible encapsulation

4.1. Introduction

The encapsulation materials have been used in many applications such as OLEDs or solar cells. Since organic layers and metal electrode which are constituent materials in devices are susceptible to moisture and oxygen, devices deteriorate in ambient air. Especially, flexible devices using plastic substrates require double-sided encapsulation (top and bottom) due to poor barrier performance of plastic substrate. Glass encapsulation with epoxy is commonly used technique, however, it is not suitable for flexible encapsulation and water vapor can diffuse through side epoxy. Direct deposition process on substrate or device can improve these disadvantages [47, 48]. The atomic layer deposition (ALD) has good step coverage and can grow highly uniform thin film. The ALD process is performed under low vacuum condition (10^{-2} Torr) and can minimize the vacuum issue when thin films are deposited directly on device [64, 65]. The ALD process can be classified as thermal and plasma-enhanced ALD (PEALD). Concisely, PEALD uses oxygen plasma as an oxidant gas instead of water vapor. Due to the high reactivity of oxygen plasma, the growth rate of PEALD is faster than thermal ALD and high dense film can be grown even at low temperature (<100℃) [68-70]. The substrate can deform at high growth temperature due to low glass transition temperature of plastic material, which is the substrate of flexible device. Therefore, low temperature process is necessary for encapsulation technology. The organic materials have high flexibility, however, high gas-permeation rate is not appropriate for encapsulation owing to large free volume. Whereas the inorganic materials have outstanding gas-barrier property (WVTR < 10^{-5} g/m^{2}day). Water vapor transmission rates which is below 10^{-5} (g/m^{2}day) are needed for OLED [56, 57]. Because water vapor diffuses through microdefects and even nanoscale defects such as grain boundary, high density amorphous structure is best structure to reach ultralow WVTR [44]. In this research, we used amorphous Al_2O_3 thin film by PEALD. The alumina thin film widely used in gas barrier-film and insulator for devices.

The amorphous alumina has many advantages as an encapsulation material, the drawbacks are low elastic limit and catastrophic failure. In previous research, the strength of ceramic materials increases as a size decreases due to size effect. The materials have pre-existed defects inside which are weak spot and reduce strength. In nanosized materials, the number of pre-existed defects reduces with size reduction and strength improves [42, 61-63].

The micro crack is formed when strain is applied above elastic limit. The material loses the function of encapsulation because water vapor diffuses through cracks. Therefore, it is important to measure the mechanical properties and estimate deformation range. In this research, we measured mechanical properties of nano-scale amorphous alumina thin film and estimated flexibility using critical bending radius.

4.2. Synthesis of amorphous Al_2O_3 thin films by PEALD at low temperature

4.2.1. Optical properties of Al_2O_3

The Al_2O_3 thin film by ALD confirms the film quality by measuring the refractive index using an Ellipsometer. After the amorphous Al_2O_3 thin film is grown on silicon substrate, refractive index and thickness are measured with an Ellipsometer. The Al_2O_3 thin film deposited at high temperature has refractive index of n ~ 1.6 and density of around 3 g/cm^3 [67, 94]. Since impurities are reduced when Al_2O_3 is deposited at high temperature, a lower refractive index is measured due to decreased density at lower temperature [67, 94]. We can calculate the density of film through Lorentz-Lorenz formula.

$$\rho = K\frac{n^2-1}{n^2+2} \tag{22}$$

Where ρ, K and n are density, constant and refractive index, respectively [68]. In this study, density of thin films was calculated by Equation 22.

For encapsulation, low temperature process is important due to heat-sensitive organic materials. Therefore, to develop a low temperature process, refractive index was measured according to growth temperature. The amorphous Al_2O_3 thin films were grown by PEALD at 80, 120 and 150℃, and the results of ellipsometer measurement are shown in Figure 4-1. As can be seen from the results, changes in refractive index and density are negligible when comparing the high and low growth temperature. It means that Al_2O_3 thin film is deposited with high density even at 80℃.

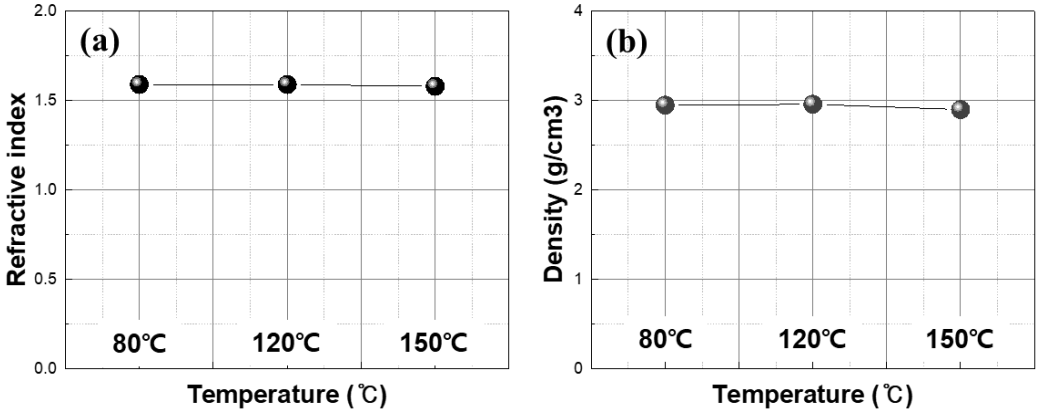

Figure 4-1. Optical properties of PEALD-Al_2O_3 thin films depending on temperature (a) Refractive index (b) Calculated density

4.2.2. Mechanical properties of Al_2O_3

Hole-nanoindentation was conducted to confirm changes in mechanical properties as well as optical properties of the Al_2O_3 thin film according to growth temperature. In case of the conventional nanoindentation, it is limited to measure the accurate properties due to the influence of the substrate in case of thin film, because sample is confined to the substrate. However, hole-nanoindentation measure the mechanical properties of free-standing films that are not bound to the substrate. The mechanical properties of the Al_2O_3 thin films are probed by indenting the center of free-standing film by hole-nanoindentation. This method has advantage that it is easier to prepare the sample than other methods.

For preparation of hole-nanoindentation sample, hole-substrate must be prepared. Hole substrate is fabricated by following step. Photoresist is spin coated on silicon substrate and patterned to the required diameter. After then, silicon is etched by deep RIE and photoresist is removed.

After transferring thin film to hole-substrate, indentation is performed. The transfer method is shown in Figure 4-3. The Cr and Au layers are deposited by sputtering on silicon substrate as adhesive and sacrificial layers, respectively. After then, Al_2O_3 thin films are deposited by PEALD. The gold layer is selectively etched by gold etchant, resulting in Al_2O_3 thin film floating in water. After the floating Al_2O_3 thin film is transferred to hole-substrate, free-standing Al_2O_3 thin films are obtained.

The hole-nanoindentation was performed in Quanta 200 SEM using PI-87 SEM Picoindenter. The Al_2O_3 thin films were grown by PEALD at 80 and 150℃ and thickness was 30 nm. Before hole-nanoindentation, it was confirmed that gold layer was completely etched through EDS. The experiments were performed with loading rate of 20 nm/s and using 5 um diameter-hole to avoid the stress concentration at hole edge. In order to obtain a more accurate average value, more than 10 experiments were conducted for each condition.

The elastic modulus can be calculated by force-displacement graph obtained using hole-nanoindentation.

$$F = \sigma_0(\pi a)\left(\frac{\delta}{a}\right) + E(q^3 a)(\frac{\delta}{a})^3 \tag{23}$$

$$q = 1/(1.05 - 0.15v - 0.16v^2) \tag{24}$$

Where F, σ_0, a, δ, E and v are applied force, pretension in the film, membrane diameter, deflection at the center point, Young's modulus and Poisson's ratio. From experimental data, σ_0 and E values are calculated by Equation 23. Also, the maximum stress at the center of film can be explained following

equation.

$$\sigma_m = \left(\frac{FE}{4\pi R}\right)^{1/2} \quad (25)$$

Where σ_m and R are the maximum stress at the central point of the film and tip radius, respectively [96]. We measured the indenter tip radius in SEM, and the radius was 90 nm. Fracture strength can be calculated by Equation 25, however, since it is an equation for elastic deformation, fracture strength can be overestimated.

As a result, fracture strength is 4.66 GPa for growth temperature of 150℃ and 4.42 GPa for growth temperature of 80℃. When comparing the fracture strength, effect of growth temperature is negligible. It means that there is no significant difference in the strength because high-dese film is deposited even at low temperature. Based on these optical and mechanical results, experiments were performed with Al_2O_3 thin films deposited at 80℃ in the subsequent study.

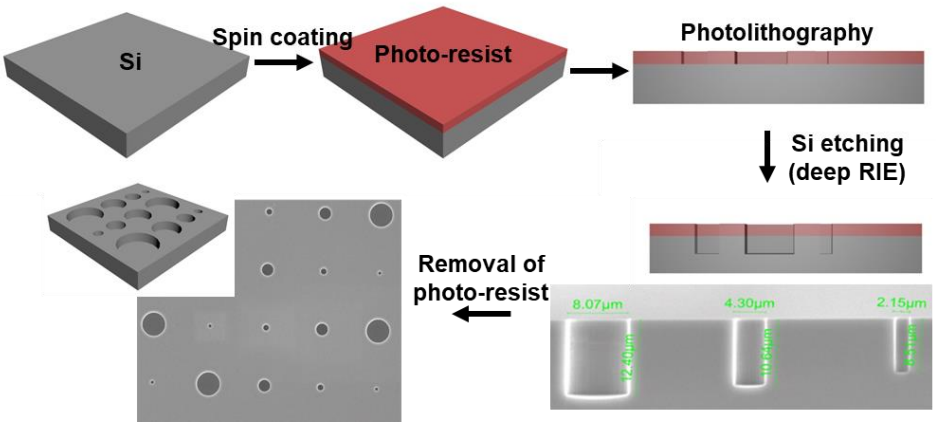

Figure 4-2. Fabrication of hole-substrate for hole-nanoindentation

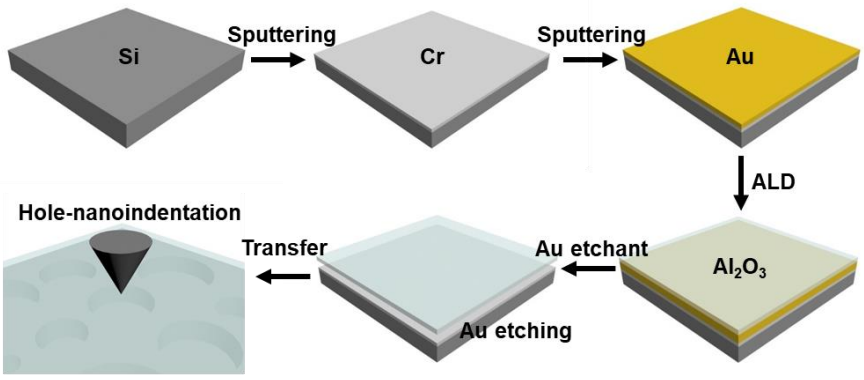

Figure 4-3. Sample preparation of hole-nanoindentation

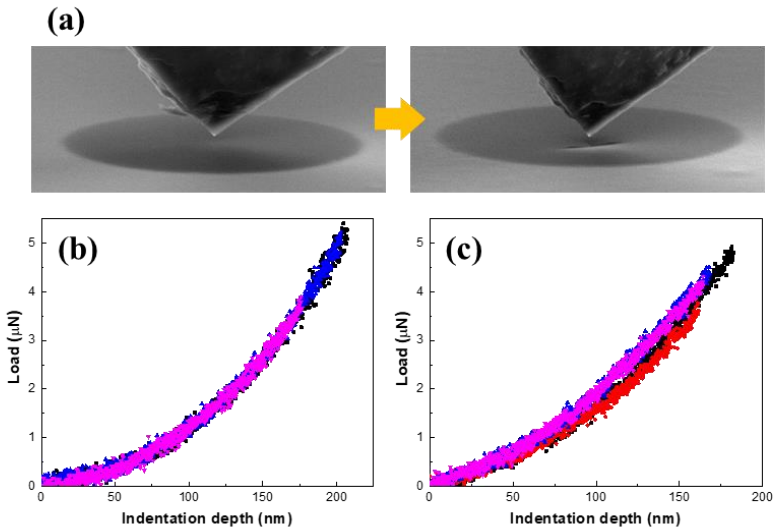

Figure 4-4. (a) Sample images of before/after fracture (b) Hole-nanoindentation results of 30 nm thick-Al_2O_3 thin films at 150℃ and (c) 80℃

4.3. Mechanical properties of Al_2O_3 films

4.3.1. Sample preparation for push-to-pull tensile test

The tensile tests were performed in order to measure accurate mechanical properties of thin films. In-situ push-to-pull tensile test was performed in Quanta 200 SEM using Hysitron PI 87 Picoindenter. Push-to-pull device is divided to moving part and fixed part. The sample is suspended from push-to-pull device and the ends of the sample is attached to the moving part and fixed part, respectively. When indenter pushes the moving part, moving part moves down and tensile strain is applied to the sample.

The fabrication methods of tensile sample are shown in Figure 4-6. Among them, general method is given in Figure 4-6 (a) (hereafter referred to as the "patterning method"). The target material is directly deposited on silicon substrate and only silicon substrate is selectively etched by XeF_2 gas. After then, material is patterned by focused ion beam instrument (FIB) with dog-bone shape and attaching the sample on the push-to-pull device using platinum. The method shown in Figure 4-6 (b) is a method of transferring material onto a push-to-pull device (hereafter referred to as the "transfer method"). Contrary to patterning method, sacrificial material and target material are sequentially deposited on substrate. Sacrificial material is selectively etched and target material is transferred to push-to-pull device. After then, material is patterned by FIB with dog-bone shape.

In this study, tensile samples were fabricated by transfer method because thickness of ALD-Al_2O_3 thin film was very thin and it was difficult to obtain free-standing film. To use patterning method, thin film should have a thickness to obtain free-standing film after silicon side etching. In case of ALD Al_2O_3 thin film, it is difficult to prepare a tensile sample in FIB because thin film sags after silicon etching when the thickness is less than 200 nm. Also, platinum can be deposited on the surface of sample gauge during the process of attaching the sample, and platinum deposited on the surface can affect the mechanical properties of nano-scale thin film. For these reason, tensile samples were prepared by transfer method. Cr and Au layer were deposited by RF sputter on silicon substrate as an adhesive and sacrificial layer. After then, Al_2O_3 thin films were grown by PEALD at 80°C. Au layer was selectively etched by Au etchant and Al_2O_3 film was transferred to push-to-pull device. Transferred Al_2O_3 film was patterned with dog-bone shape in focused ion beam.

After sample preparation, we confirmed that residual gold was not remained in Al_2O_3 thin film. In addition, it was confirmed that there was no sliding phenomenon between Al_2O_3 film and silicon device without Pt adhesion during tensile test.

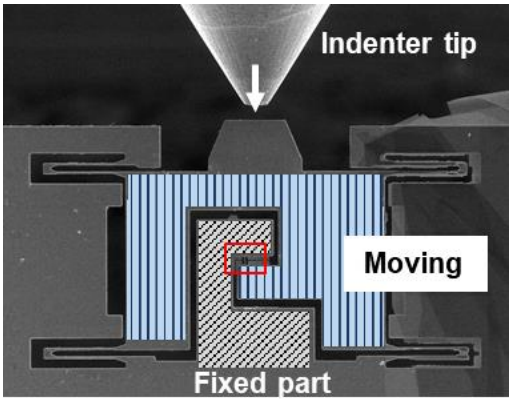

Figure 4-5. Tensile test using push-to-pull device

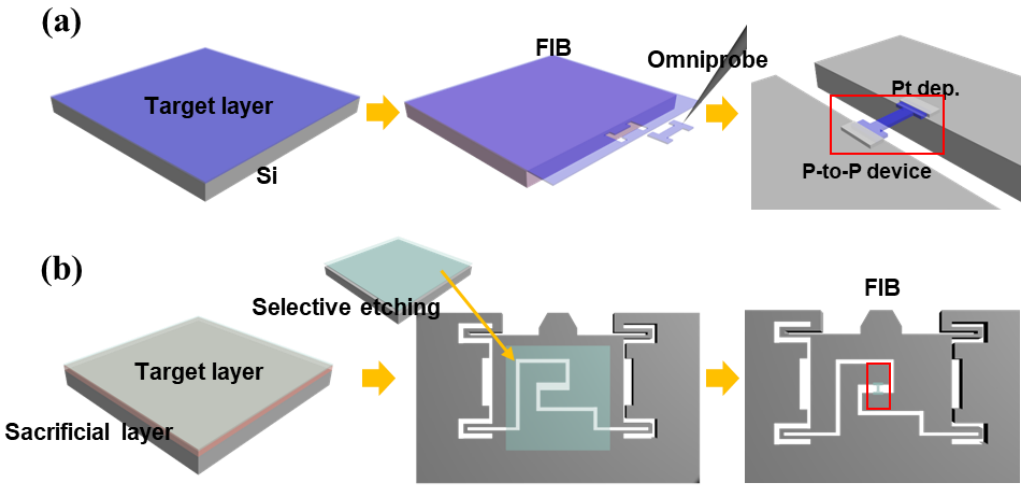

Figure 4-6. Fabrication method of tensile test sample (a) Patterning method (b) Transfer method

4.3.2. Plastic deformation by e-beam irradiation

Zheng et al. [97] reported that amorphous silica shows plastic deformation in TEM. The compressive and tensile test were performed using amorphous silica particle and nanowire. Both of compression and tension, amorphous silica had electron-beam-assisted plastic deformation at room temperature. The Si-O bonds are broken by e-beam radiation and dangling bonds are formed in amorphous silica. As a result of simulation, these dangling bonds reforms bonding with other non-bridge atoms, resulting in bond-switching and plastic flow. In previous research, brittle ceramic materials show plastic deformation in very thin nanowire by surface diffusion. However, plastic flow is induced by e-beam irradiation even in small surface to volume ratio samples.

Qu et al. [98] reported that damage recovery is induced by e-beam in silicon film. In this study, silicon films with nanoscale-hole damage by FIB are focused on the electron beam and damage recovery is observed in TEM. As a result, hole-damage is recovered by amorphization. The hole diameter becomes small and the edge of hole is amorphized, and the hole completely recovers. After damage recovery, amorphous structure recrystallizes at a relatively low electron flux. Under high energy e-beam condition, silicon structure can be distorted locally, resulting in amorphization and crystallization.

Mackovic et al. [99] reported that silica nanoballs are densified and show plasticity by e-beam irradiation. They prepared silica nanospheres exposed to high and low current density beam in TEM. After beam irradiation, sphere diameter is reduced by densification. As a result of compressive tests, when the compressive displacement is fixed, maximum load of high-dose irradiation sample is higher than that of low-dose irradiation sample under beam-off condition. However, maximum load is reduced and plastic deformation is occurred under beam-on condition. According to this paper, e-beam not only causes plastic deformation of the amorphous silica sphere, but also densification.

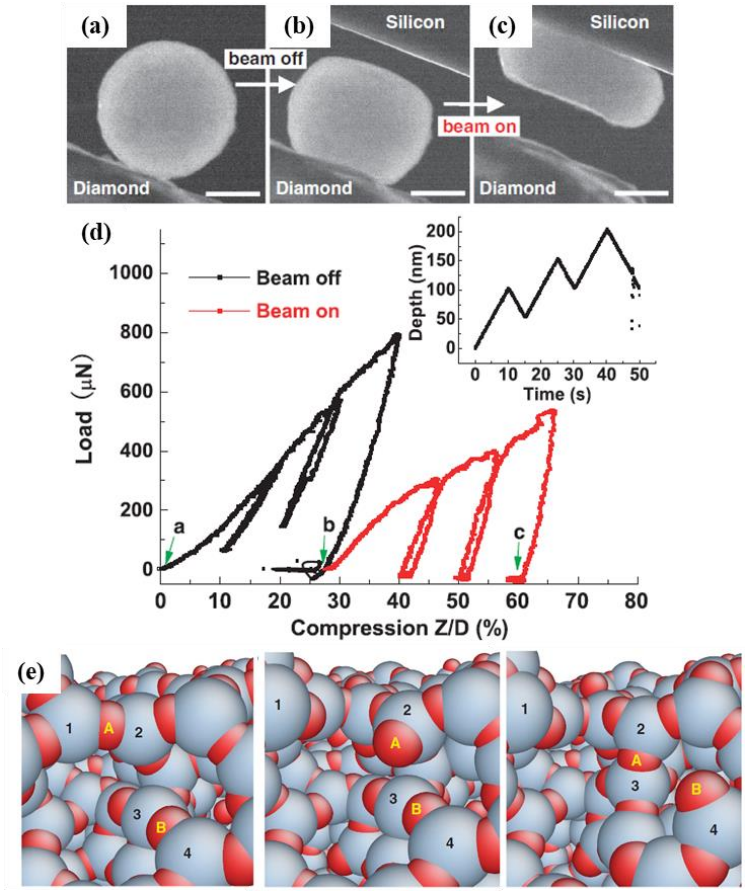

Figure 4-7. (a) Compression of silica particles (b) Under beam off (c) Beam on condition (d) Compression graph of beam on/off (e) Mechanism of atomic bond switching [97]

4.3.3 Tensile properties of Al_2O_3 thin films

Tensile tests were performed in SEM and mechanical properties were analyzed as thickness decrease. The Al_2O_3 thin films have plastic deformation and elastic modulus is reduced in SEM due to beam penetration. When electron beam is penetrated in thin film, Al-O bond is broke and dangling bonds were formed [97]. The bonding energy of Al and oxygen is 5.3 eV and threshold displacement energy of Al and oxygen is 32 eV and 50 eV, respectively [100, 101]. Therefore, enough dangling bonds which are applied plastic deformation can be formed in thin films. Those dangling bonds are moved as combining neighbor atoms when tensile deformation is applied. As a result, elastic limit increases and elastic modulus is reduced [97]. In our research, measurement of intrinsic tensile properties of Al_2O_3 thin films is important. Therefore, experiments were performed in beam off condition for excluding beam effect. Samples were aligned in 10 keV beam condition and tests were performed after 15 min beam off. As a result, Al_2O_3 thin films have only elastic deformation.

They all show linear elasticity, negligible plasticity, and catastrophic failure. Figure 4-9 (b) shows SEM images for initial sample and the sample after failure. The moving part in the push-to-pull device returned to initial position by removing external force after the failure. Fractured upper and bottom gauge sections are in alignment without distortion or overlap, which indicates that plasticity was negligible in the tensile testing. The average of elastic modulus is about 180 GPa similar with previous reports which grown at high temperature (>100℃) [79, 102-105]. Due to density reduction, elastic modulus decreases as growth temperature decreases [79]. However, our films have similar mechanical properties with high growth temperature deposition films because quality of Al_2O_3 films is similar with other results. The fracture strength of 200, 100, 50 nm thickness is 4.32 (±0.12), 4.41(±0.14) and 4.45 (±0.03) GPa and fracture strain is 2.90(±0.05), 3.01(±0.19) and 3.09% (±0.01), respectively.

Our Al_2O_3 films do not show size effect in strength, that is increase in strength with decreasing the sample thickness. By the Griffith's theory, tensile fracture strength increases as the sample thickness decreases due to lower probability for containing defects acting as stress concentrators, and tensile fracture strength is independent of the sample thickness below the critical thickness (i.e. not follow the Griffith criteria) because material becomes insensitive to intrinsic defects [63]. In case of amorphous Al_2O_3 thin film by PEALD, size comparison of intrinsic defects is not big because ALD process grow up high uniform and dense films regardless of thickness. The defect size can be estimated by Griffith equation [106]. Using our tensile results, size of intrinsic defects is 2.27 nm for 50 nm thick-thin film, 2.30 nm for 100 nm thickness and 2.59 nm thickness. The defect size is not so different, and negligible for fracture strength. The tensile stress-strain results support that the Al_2O_3 films deposited by PEALD at 80℃ are high-dense and contain rare defects.

4.3.4 Critical bending radius

Based on tensile results, critical bending radius (R) which is crack formation radius is calculated using equation. The strain applied to thin film encapsulation under bending deformation is expressed by Equation (26).

$$\varepsilon = (\frac{t-t_n}{R}) \tag{26}$$

Where t and t_n are total thickness and neutral plane position (i.e. strain-free plane), respectively. When the elastic modulus of film and substrate are similar, neutral plane is located at the mid-surface, and strain and critical bending radius can be expressed by following equation.

$$R = \frac{t}{2\varepsilon} X100 \tag{27}$$

Equation (27) is consider only thickness (sum of substrate and film thickness).

$$R = \frac{t(1+2b+ab^2)}{2\varepsilon(1+b)(1+ab)} \tag{28}$$

$$a = E_f/E_s\,,\ b = t_f/t_s$$

Where E_f, E_s, t_f and t_s are elastic modulus of film and substrate and thickness of film and substrate, respectively. i.e. a and b are ratio of elastic modulus and ratio of thickness. Equation (28) is consider thickness and elastic modulus both [107].

As a calculation results, critical bending radius of 50 nm thick-Al_2O_3 thin film on PET substrate is 2.02 mm and 1.97 mm when using Equation (27) and (28), respectively. There is no big difference between the two values. Because the thickness of PET substrate is very thick compared to the Al_2O_3 thin film, difference of elastic modulus is negligible. Based on calculated critical bending radius, cyclic bending tests were performed with 2 mm bending radius. As you can see in Figure 4-12, crack propagation is occurred in Al_2O_3 film after 1,000 cycles bending at 2 mm bending radius. This sample lose the barrier performance as an encapsulation material due to micro cracks.

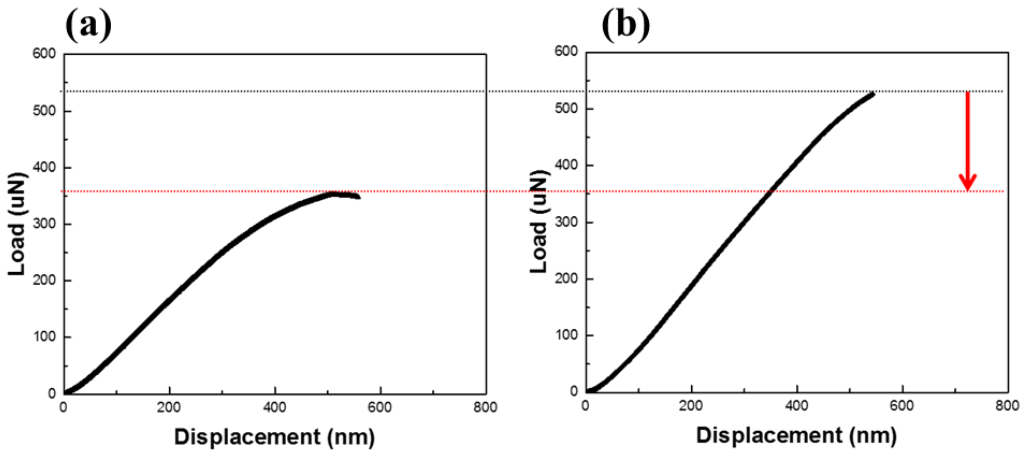

Figure 4-8. Tensile test results of 100 nm thick-Al_2O_3 thin films (a) Beam on (b) Beam off condition

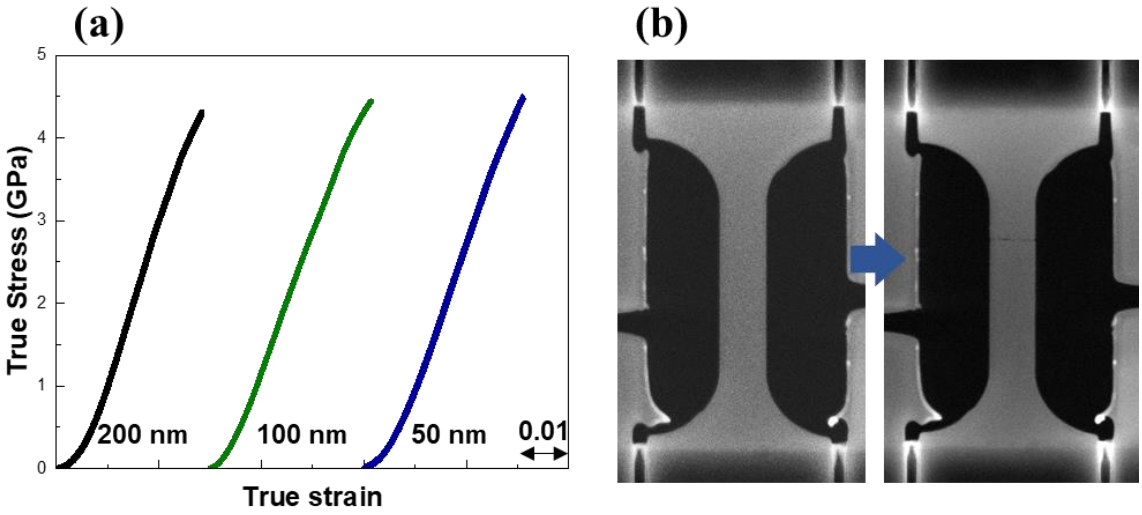

Figure 4-9. (a) Stress-strain curves of PEALD-Al_2O_3 thin films (b) SEM images of before and after fracture

4.4. WVTR of Al_2O_3 film after cyclic bending

4.4.1. WVTR of single Al_2O_3 layer

We performed electrical calcium tests for WVTR measurement. Cr and Au layer are used as an adhesion and electrode layer on glass substrate. Calcium was deposited on electrode using thermal evaporator in glove box. For sample preparation, 50 nm thick-Al_2O_3 thin films were deposited on PET substrate and samples were attached to glass using epoxy (LOCTITE E-30CL). For epoxy aging, samples are kept in glove box for 24 hours. Since water vapor diffusion rate is so slow at ambient condition, calcium tests were performed at 60°C and 85% RH condition. Figure 4-10 (b) is typical time-to-conductance graph of 50 nm thick-Al_2O_3 thin film. The WVTR value is fitted linearly at steady state region. As a result, 50 nm thick-Al_2O_3 thin film WVTR is 3.21 X 10^{-4} (±0.00027) g/m^2day.

4.4.2. WVTR of Al_2O_3 film after cyclic bending

Based on calculated critical bending radius, cyclic bending tests were performed with 2 mm bending radius. As you can see in Figure 4-12, crack propagation is occurred in Al_2O_3 film after 1,000 cycles bending at 2 mm bending radius. This sample lose the barrier performance as an encapsulation material due to micro cracks. We conducted cyclic bending test at 10 mm radius and micro crack was not observed after 1,000 cycles bending in OM. However, WVTR is 8.71 X 10^{-4} g/m^2day which is 2.5 times greater than raw WVTR values. As a result of 10,000 cycles bending, WVTR results are 1.07 X 10^{-3} g/m^2day which is 3.3 times greater than raw WVTR. At 20 mm radius, change of WVTR is negligible until 50,000 cycles bending. However, WVTR graph of 50,000 cycles bending has two linear regions after transient region. The WVTR of first and second linear region is 3.84 X 10^{-4} g/m^2day and 1.64 X 10^{-4} g/m^2day, respectively. As a result of 100,000 cycles bending at 20 mm radius, WVTR is 1.69X10^{-3} g/m^2day. It means that defect density increases as bending cycle increases and material has other diffusion paths except for microcrack. In addition, this indicates that any defects acting as a high diffusion path of the water vapor are gradually formed by the cyclic bending with a bending radius greater than the critical bending radius evaluated by the stress-strain curves even though crack-like defects are not formed by the cyclic bending.

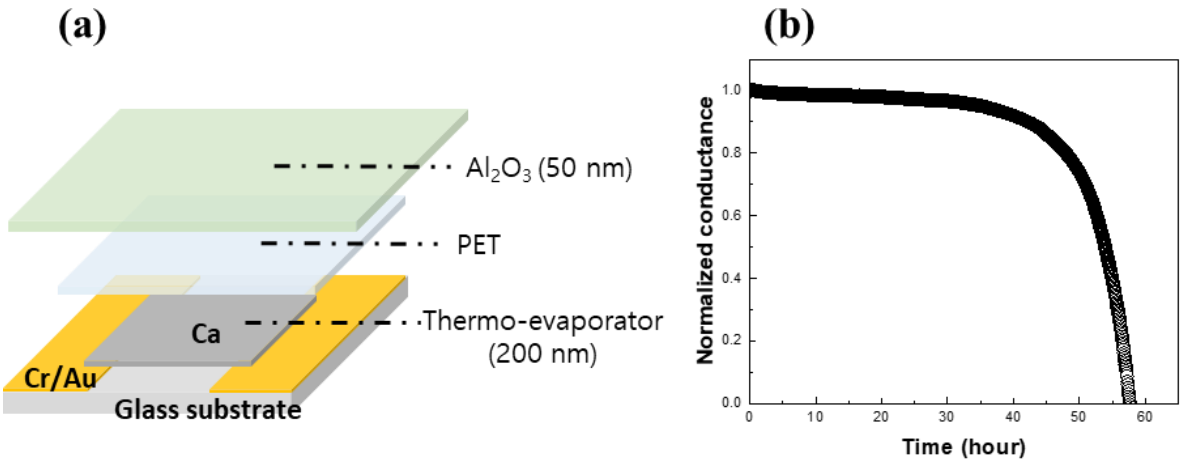

Figure 4-10. (a) Calcium kit of electrical calcium test (b) Typical WVTR graph of 50 nm thick-Al_2O_3 thin film

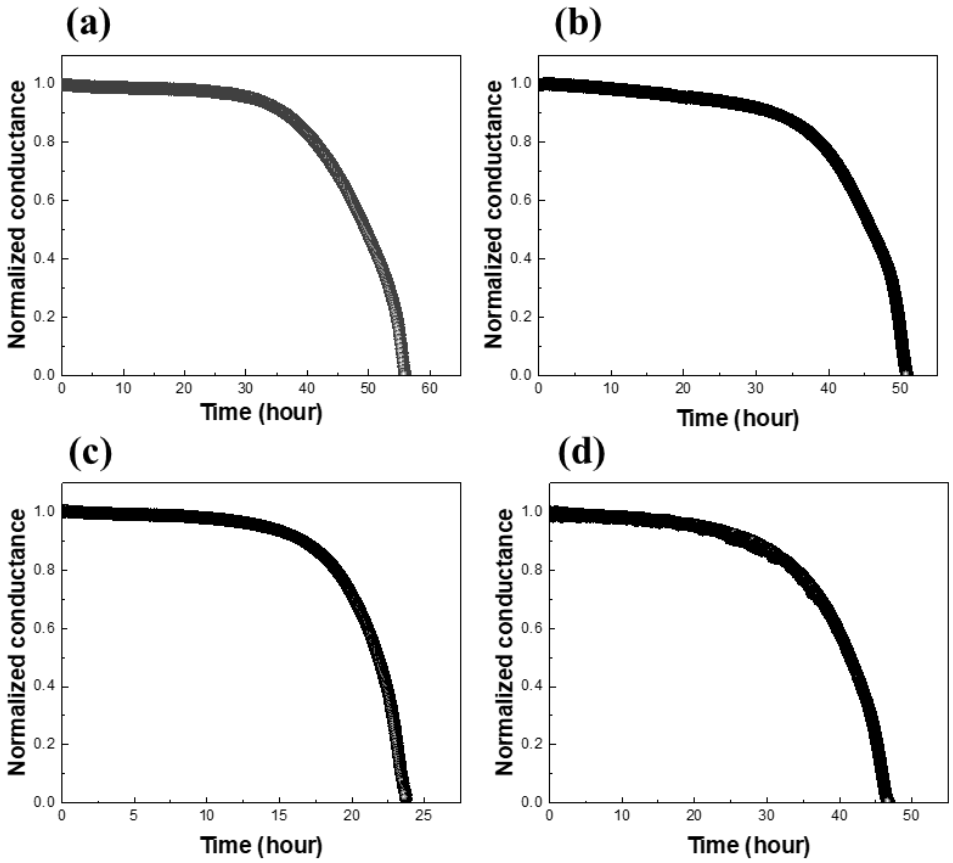

Figure 4-11. Typical WVTR graph after cyclic bending (a) 1,000 cycles at R 10 mm (b) 50,000 cycles at 20 mm (c) 100,000 cycles at 20 mm (d) 100,000 cycles at 25 mm

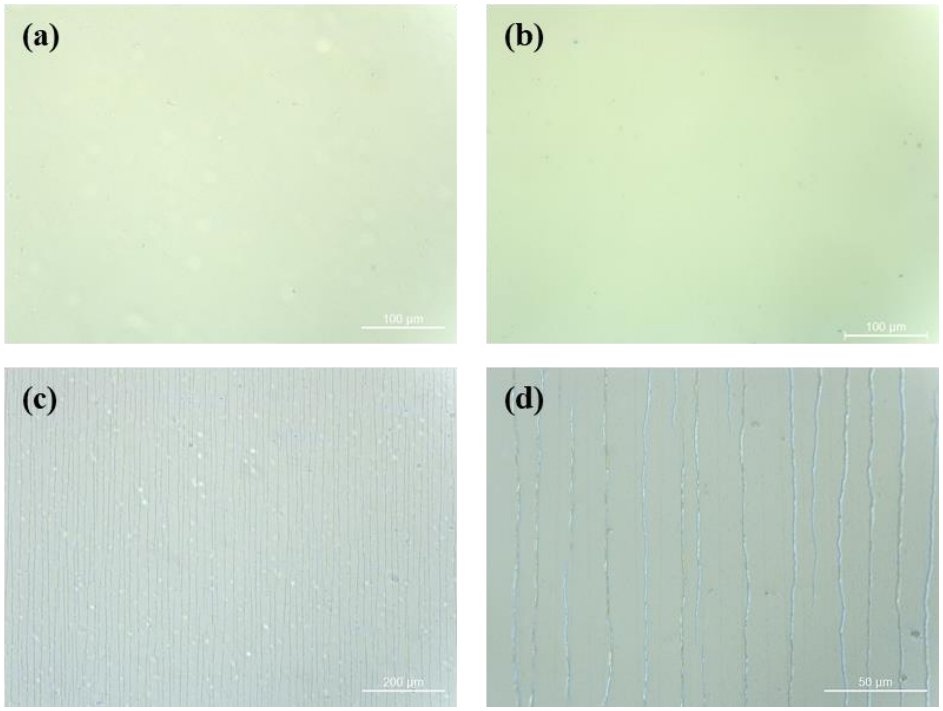

Figure 4-12. Optical microscope images of 50 nm thick-Al_2O_3 thin films on PET (a) Before bending (b) After 1,000 cycles bending at 10 mm (c) and (d) Low and high magnitude after 1,000 cycles bending at 2 mm

4.5. Mechanism of WVTR degradation

4.5.1. Atomic bond-switching in amorphous oxide

Bonamy et al. [108] observed crack propagation mechanism of silica glass within the stress concentration zone at the crack tip by atomic force microscopy (AFM). In general, brittle materials are known that cracks are sequentially grown from the crack tip because stress is concentrated at the front of the crack tip. In simulation results, crack propagates through nucleation and coalescence of nanoscale-cavities. To confirm this plastic flow, crack growth of notched samples by stress corrosion tests was observed by AFM. As a result, nanoscale-cavities are formed within stress concentration zone, and fracture is induced by coalescence of these cavities. i.e. bonds break in low density region and these cavities act as stress concentrator, causing microcrack propagation.

Luo et al. [109] reported that amorphous brittle silica becomes to ductile as thickness decreases at room temperature. The tensile tests are conducted under beam-off condition in order to except for electron beam effect and diameter of amorphous silica nanofibers is 1 to 50 nm. As a result of tensile tests, plastic deformation occurs when diameter of nanofiber is below 18 nm. The silica nanofibers have brittle failure when diameter is greater than 18 nm, while elongation increases as diameter decreases below 18 nm. In the near surface region, many dangling bonds (i.e. non-bridge oxygen or broken silicon bonds) exists and these can accelerate bond-switching. When the deformation is applied to nanofiber, dangling oxygen bond moves to closest silicon atom and forms new Si-O bond. The bond-switching also occurs inside material, but most bond-switching is induced by surface assist. As the diameter decreases, the surface-to-volume ratio increases, resulting in plastic flow.

In simulation results, amorphous silica nanofibers have ductility and ductility is enhanced by damage accumulation. Bonfanti et al. [110] reported MD simulation results according to diameter size of silica nanofiber. As diameter decreases, elongation is enhanced due to stress drop. Stress drop is caused by bond-breaking which induces damage accumulation. This study suggests that surface diffusion is not the only mechanism for brittle-to-ductile transition. In small diameter, the material is broken by the coalescence of disorder-induced cracks.

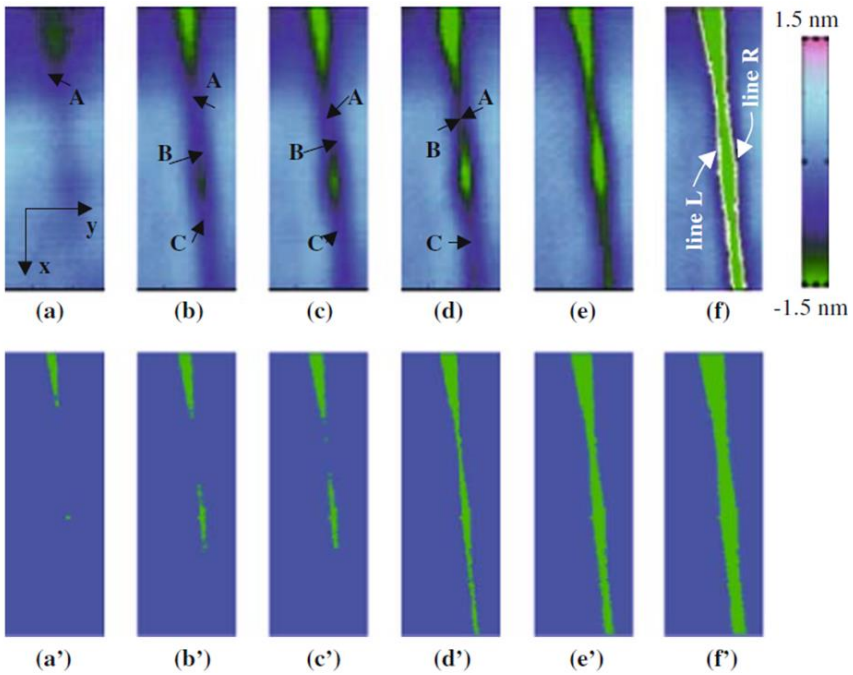

Figure 4-13. Crack propagation at the notch tip [108]

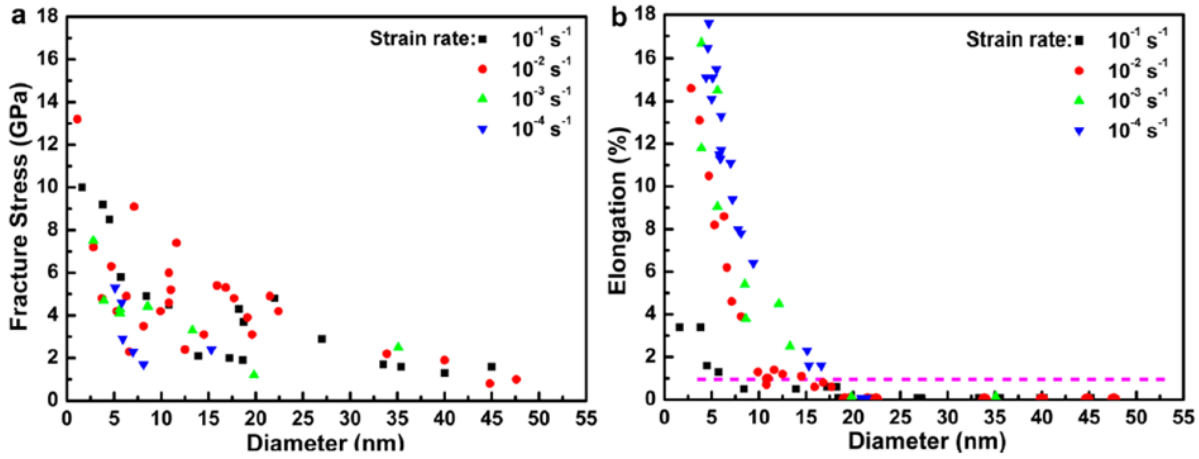

Figure 4-14. Sample size and strain-rate dependence (a) Fracture strength (b) Elongation [109]

4.5.2. Optical calcium test

This issue can be explained by pinhole formation. Because micro crack is not formed after cyclic bending, water vapor diffuses through nano-scale defects which cannot be seen in OM image. Water vapor size is about 3Å [43, 44] and nano-scale defects can be diffusion path sufficiently. The tensile stress is applied at the top of samples above the neutral plane under bending deformation. So, crack is formed and propagated through thin film due to stress concentration. The thin film is completely recovered after unloading under elastic limit. In previous simulated and experimental results, plastic deformation is occurred in atomic scale even ceramic materials such as SiO_2 and Al_2O_3. The dangling bonds which are intrinsic defects in the materials are moved and combined with neighboring atoms. As a result, atomic bond-switching is occurred and this local plastic deformation leads to structural rearrangement [108, 109, 111]. We knew that amorphous alumina has greater potential for bond-switching than amorphous silica from previous paper [111]. Since tensile deformation of oxide materials occurs through perpendicular to the loading direction, we can estimate that nano-scale pinholes are formed through thickness direction [110].

To prove this hypothesis, we conducted optical Ca tests and observed aspects of oxidation over time. Unlike electrical Ca test, free volume is not required in optical Ca kit. After Al_2O_3 deposition on PET, calcium square was directly deposited on Al_2O_3 layer to observe the moisture diffusion path. The other side was encapsulated by glass with epoxy (LOCTITE E-30CL). For epoxy aging, the calcium kit was kept in glove box over 24 hours. For cyclic bending samples, calcium was deposited on Al_2O_3 samples after cyclic bending. The optical calcium tests were performed at 85℃ and 85% RH condition to accelerate the moisture movement and optical microscope images were obtained under ambient condition.

Figure 4-16 shows oxidation aspects of 50 nm Al_2O_3 thin films before bending, after 1,000 cycles bending at 10 mm radius and after 100,000 cycles bending at 20 mm radius. The oxidation is initiated at certain point within 1 hour after 1,000 cycles bending at 10 mm radius. In case of the pristine Al_2O_3, oxidation was not occurred even after 6 hours. These results can be evidence for formation of pinholes which are water vapor diffusion path in the material instead of microcracks. The sample which is after 100,000 cycles bending at 20 mm radius has smaller and more pinholes than sample which is after 1,000 cycles bending at 10 mm radius. Since applied strain is so small at 20 mm bending radius, bond-switching is not occurred at initial low bending cycles. However, local damage is accumulated and nano-size defects are formed [111] around 50,000 cycles. The relatively small size pinholes which can be affected WVTR are formed around 100,000 cycles. The reason why oxidation aspects are different between 10 mm and 20 mm bending radius, applied strain on the material is different as a bending radius. Since applied strain at 10 mm bending radius is greater than 20 mm bending radius, larger pinholes are generated. In addition, the number of pinholes is relatively small and the WVTR

value is low due to 100 times less bending cycle. WVTR value does not change even after 100,000 cyclic bending at 25 mm bending radius. We also confirmed that encapsulated Ca oxidation is similar to pristine sample.

In previous research, defect density was analyzed depending on bending radius and the number of cycles. Patel et al. [112] observed defect density of plasma-deposited inorganic thin films on flexible substrate by optical microscope. Since PC substrate is etched by acetone, after thin film deposition, when exposed to acetone, the point etched by the defect can be observed. As a result of cyclic bending, defect density increases as bending radius decreases and the number of cycles increases.

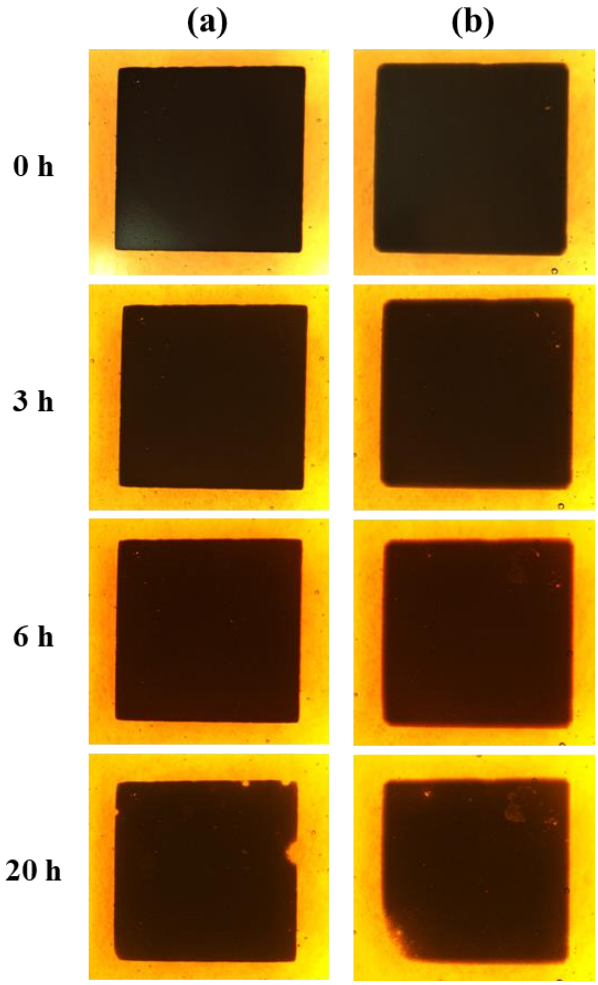

Figure 4-15. Optical calcium tests (a) Before bending (b) After 100,000 cycles bending at R 25 mm

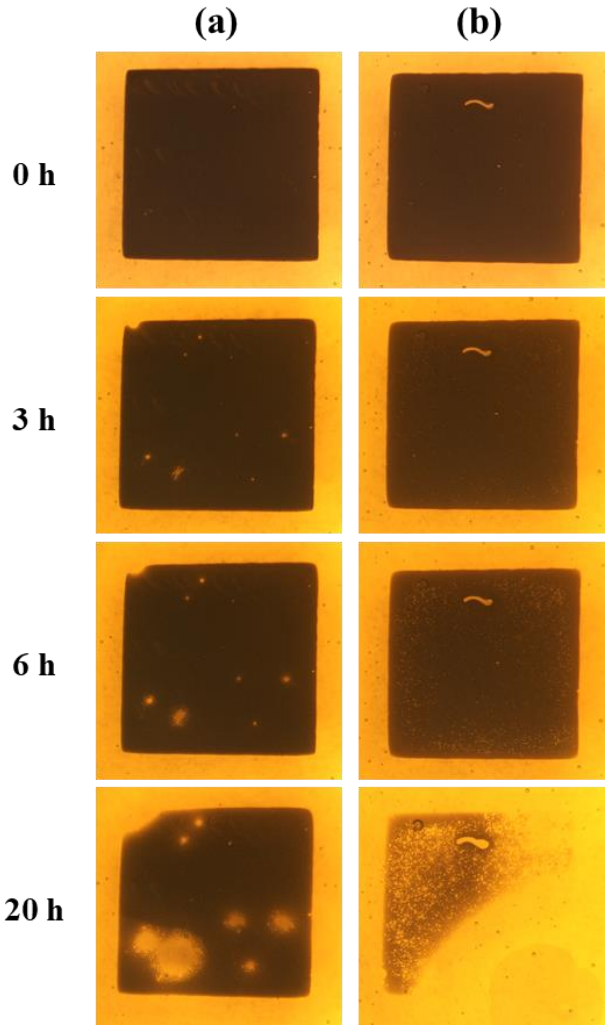

Figure 4-16. Optical calcium test (a) After 1,000 cycles bending at R 10 mm (b) After 100,000 cycles bending at R 20 mm

4.6. Application

4.6.1. Optical Mg test

The commonly used encapsulation method uses glass and epoxy as top and side encapsulation, respectively. This method is to attach the glass lid to the device using epoxy. However, the side epoxy seal has poor barrier performance and device deteriorates from the edge due to water vapor side diffusion. To avoid this issue, this study introduced ALD process prevent side penetration of moisture by depositing a uniform thin film over the entire device without the use of epoxy in this study.

Before applying to the device, we confirmed the side penetration of moisture through optical magnesium tests. Since magnesium is sensitive to moisture, it reacts with moisture to cause oxidation. When magnesium is oxidized, we can observe the oxide formation visually through color change. We prepared two types of magnesium kits. The process of optical magnesium kit is as follow. Magnesium is deposited on SiO_2 substrate by RF sputtering. Thickness of magnesium is 300 nm which is the thickness of typical organic device. After then, 25 nm thick-Al_2O_3 is directly deposited on magnesium. The other kit was made by coating a polymer on magnesium. 4 um thick-NOA 61 was coated on magnesium by spin coating, and Al_2O_3 was deposited. NOA 61 was cured by UV lamp. Optical magnesium tests were performed at 85℃ and 85% RH condition to accelerate the moisture movement and optical microscope images were obtained under ambient condition. The oxidation aspects were observed by OM images of edge and center of magnesium.

As a result, oxidation started after 10 hours within magnesium. The oxidation progressed in a new point or the oxide film gradually increased from the initial oxidation point. As a result of this, it was confirmed that the side penetration was improved because the Al_2O_3 thin film was uniformly deposited in the thickness direction by PEALD. Oxidation of polymer coated kit also started within magnesium. It means that Al_2O_3 thin film can be uniformly deposited even in the microscale thickness direction by PEALD.

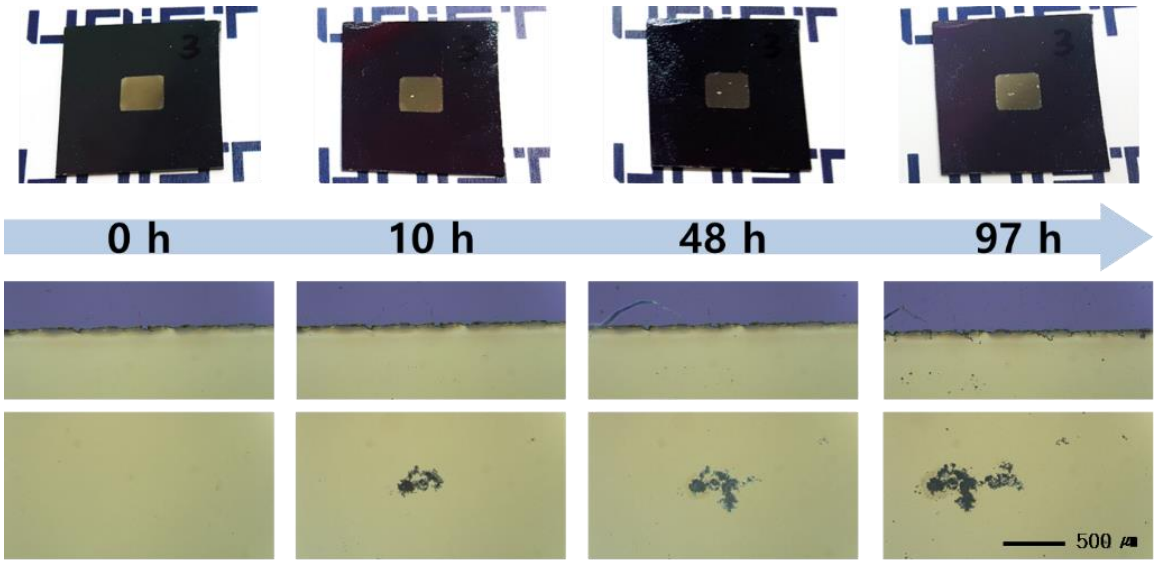

Figure 4-17. Optical magnesium tests encapsulated by 25 nm thick-Al_2O_3 at 85℃, 85% RH

4.6.2. Perovskite solar cell encapsulation

Hybrid organic-inorganic halide perovskite solar cells (PSCs) are based on methylammonium lead iodide ($CH_3NH_3PbI_3$). Perovskite solar cells have advantages of high power conversion efficiency (PCE), cost-effective materials and manufacture process [11]. However, stability issue is a major problem in commercializing PSCs. Perovskite is sensitive to water vapor and oxygen, and efficiency degrades under ambient condition [113, 114]. When $CH_3NH_3PbI_3$ is exposed to water vapor, color changes from dark brown to yellow due to formation of PbI_2. $MaPbI_3$ degradation mechanism by water vapor is shown in Equation (29) and (30) [113-115].

$$CH_3NH_3PbI_3 + H_2O \leftrightarrow CH_3NH_3PbI_3{\cdot}H_2O,\ (CH_3NH_3)4PbI_6{\cdot}2H_2O \quad (29)$$

$$CH_3NH_3PbI_3{\cdot}H_2O \rightarrow PbI_2 + CH_3NH_3I + H_2O \quad (30)$$

To improve stability of perovskite solar cell, exposure of water vapor is prevented by encapsulation. In this study, perovskite solar cell was encapsulated by PEALD-Al_2O_3 and PCE was measured over time. Before encapsulation, temperature tests were performed in glove box. Perovskite solar cells were heated at 30℃ (here after called as reference cell) and 60℃ (hereafter called as heated cell) under dark condition and efficiency was measured in ambient condition. In glove box, PCE of reference cell increased slightly and was maintained for 7 days. Meanwhile, PCE of heated cell was halved in a week. Based on these results, accelerated testing was performed at 30℃, 90% RH condition.

In this research, PSC is encapsulated using PEALD-Al_2O_3 thin film and accelerated tests were performed in 30℃, 90% RH under dark condition. The efficiency of PSC retains and gradually reduces after 27 days. In general, PSC color changes and efficiency drop rapidly when reacts with water vapor. As shown in Figure 4-18, color of encapsulated PSC changed from dark brown to light color due to water vapor, while PCE decreased rapidly. However, in Figure 4-19, perovskite color did not changed and efficiency gradually decreased after 100 days.

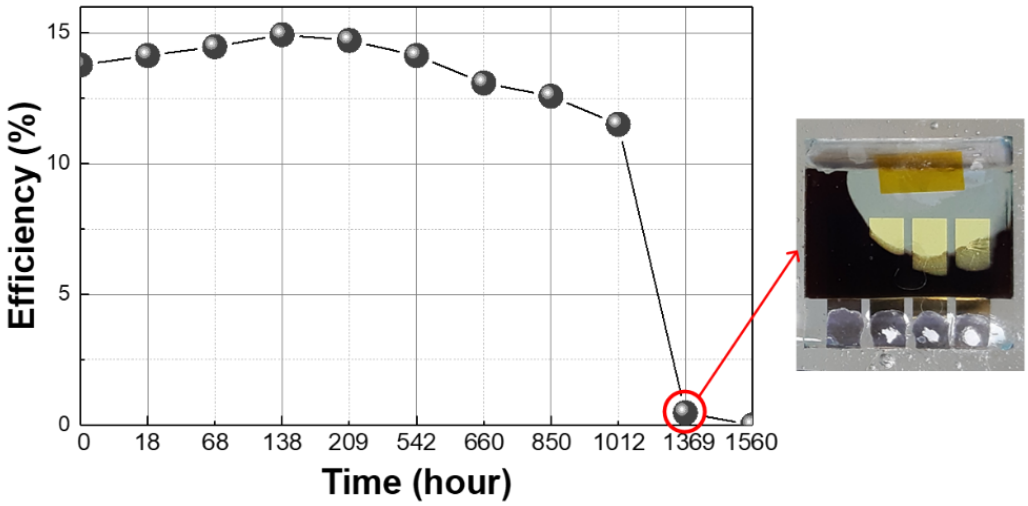

Figure 4-18. Efficiency of encapsulated perovskite solar cell under 30℃, 90% RH

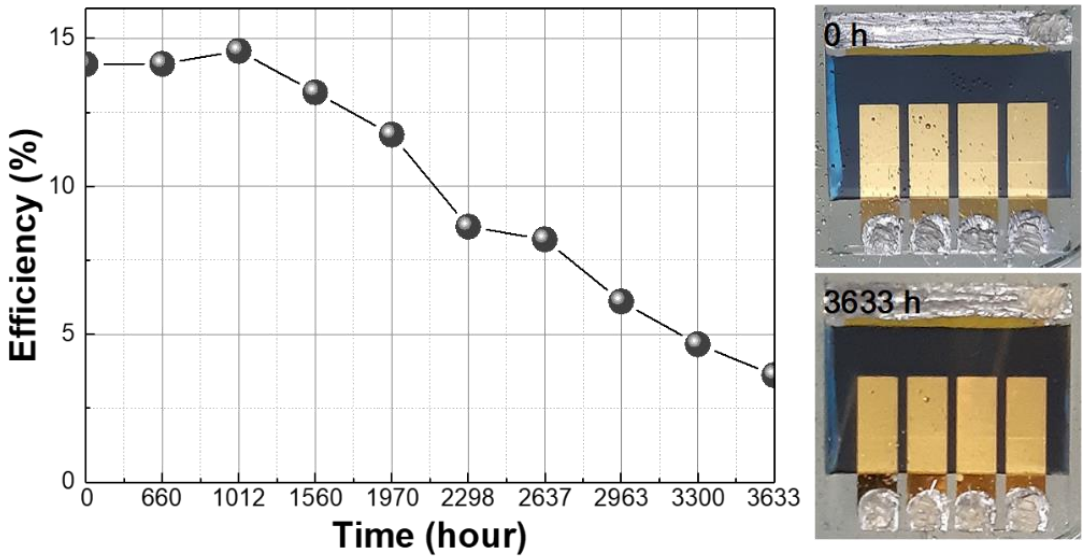

Figure 4-19. Efficiency of encapsulated perovskite solar cell under 30℃, 90% RH

4.7. Conclusion

In this research, we developed the PEALD process at low temperature for Al_2O_3 thin film encapsulation. Refractive index was measured by ellipsometer, and density was calculated by Lorentz-Lorenz equation. As a result, Al_2O_3 thin films grown at 150℃ and grown at 80℃ have similar density. In addition, hole-nanoindentation was conducted to confirm mechanical properties depending on growth temperature. Fracture strength is 4.66 GPa for growth temperature of 150℃ and 4.42 GPa for growth temperature of 80℃. It means that high dense Al_2O_3 thin film can be deposited even at low temperature.

In order to enhance the flexibility, in-situ tensile tests were performed to measure the mechanical properties of Al_2O_3 thin films according to thickness based on Griffith's theory. Fracture strength and fracture strain of 50 nm thick-Al_2O_3 thin film are 4.45 GPa and 3.09%, respectively. Based on tensile results, calculated critical bending radius was ~2 mm when 50 nm Al_2O_3 thin film is deposited on 125 um thick-PET substrate.

To evaluate encapsulation performance, electrical calcium tests were performed at 60℃, 85% RH condition. WVTR of 50 nm thick-Al_2O_3 thin film was $3.21X10^{-4}$ g/m^{2}day. We conducted cyclic bending test at 10 mm and 20 mm radius and micro crack was not observed in OM. However, WVTR of 1,000 cycles bending with 10 mm radius and 100,000 cycles bending with 20 mm radius is 8.71 X 10^{-4} g/m^{2}day and $1.69X10^{-3}$ g/m^{2}day, respectively. i.e. WVTR degradation was observed even after cyclic bending at radius greater than critical bending radius. This degradation mechanism was described in bond-switching, and optical calcium test was performed as an evidence. WVTR value was maintained after 100,000 cycles bending at 25 mm bending radius.

5. Summary

Flexible solar cells have been widely studied to improve flexibility and efficiency. Among the various types of solar cells, crystalline silicon (Si) solar cells are widely used owing to their high energy-conversion efficiency and application feasibility. However, flexibility improvement is important due to brittle fracture, and flexibility is reduced by surface texturing. Therefore, flexibility can be improved through mechanical properties analysis according to surface texturing. In case of organic based solar cells, they have excellent flexibility due to highly flexible constituent polymer, but encapsulation is required owing to their poor stability in air. As an encapsulation material, inorganic materials are used to effectively prevent the penetration of water vapor. To improve the flexibility of the encapsulation material, we evaluated the optimum thickness with low permeability and high flexibility. We evaluated the mechanical properties of inorganic materials through various methods to enhance the flexibility.

By this dissertation, surface texturing effects on flexural properties were analyzed by 4-point bending test. We prepared non-, dome-, pyramid-textured ultra-thin silicon. Flexural strength was measured by bending test and Weibull distribution was used for statistical analysis of flexural strength. Flexural strength and characteristic strength of surface textured silicon were lower than that of non-textured silicon. Also, strength distribution of surface textured silicon is narrower than that of non-textured silicon. Through these results, we found that the surface texturing affects strength reduction because surface structures act as defects, stress concentrator. The geometrical factors affecting the stress concentration factor are as follows : (1) notch angle, (2) depth of notch and (3) radius of notch tip. Based on these factors, stress concentration enhanced in pyramids with larger notch depth and smaller notch tip, resulting in lower flexural strength. The critical bending radius also increases in the order of non-, dome-, and pyramid textured samples and optical reflectance of dome-textured silicon is lower than that of pyramid-textured silicon. In conclusion, dome texturing shows better performance than pyramid texturing in terms of efficiency and flexibility.

In this research, we developed flexible encapsulation material and evaluated the mechanical behavior by cyclic deformation. In order to enhance the flexibility, in-situ tensile tests were performed in SEM to measure the mechanical properties of Al_2O_3 thin films according to thickness based on Griffith's theory. Fracture strain of 50 nm thick-Al_2O_3 thin film is 3.09%. Based on tensile results, critical bending radius was calculated and value was around 2 mm when 50 nm Al_2O_3 thin film is deposited on 125 um thick-PET substrate. The factors affected bending radius are as follows : (1) thickness of film and substrate, and (2) elastic modulus of film and substrate.

WVTR value which implies encapsulation performance degraded even after cyclic bending at radius greater than critical bending radius. Micro cracks were not observed in OM images of samples that were cyclic bent at radius greater than 2 mm. We determined the formation of water vapor diffusion path other than micro cracks. Pinhole formation mechanism was described in bond-switching, and optical calcium test was performed as an evidence. In addition, we found that WVTR value was maintained even after 100,000 cycles bending at 25 mm bending radius.

REFERENCES

1. Ramanathan, V.; Feng, Y., Air pollution, greenhouse gases and climate change: global and regional perspectives. *Atmospheric Environment* **2009,** *43* (1), 37-50.

2. Zuberi, M. J. S.; Ali, S. F., Greenhouse effect reduction by recovering energy from waste landfills in Pakistan. *Renewable and Sustainable Energy Reviews* **2015,** *44*, 117-131.

3. Zhou, Y.; Hu, J.; Wu, Y.; Qing, R.; Zhang, C.; Xu, X.; Jiang, M., Review on methods for improving the thermal and ambient stability of perovskite solar cells. *Journal of Photonics for Energy* **2019,** *9* (04).

4. Armaroli, N.; Balzani, V., The future of energy supply: Challenges and opportunities. *Angewandte Chemie-International Edition* **2007,** *46* (1-2), 52-66.

5. Almansouri, I.; Ho-Baillie, A.; Green, M. A., Ultimate efficiency limit of single-junction perovskite and dual-junction perovskite/silicon two-terminal devices. *Japanese Journal of Applied Physics* **2015,** *54* (8S1).

6. Shah, A. V.; Schade, H.; Vanecek, M.; Meier, J.; Vallat-Sauvain, E.; Wyrsch, N.; Kroll, U.; Droz, C.; Bailat, J., Thin-film silicon solar cell technology. *Progress in Photovoltaics: Research and Applications* **2004,** *12* (23), 113-142.

7. Kashyap, K.; Kumar, A.; Yang, C.-Y.; Hou, M. T.; Yeh, J. A. In silicon substrate strength enhancement depending on nanostructure morphology, *Proceedings of the 9th IEEE International Conference on Nano/Micro Engineered and Molecular systems* **2014**.

8. Wilson, C. J.; Ormeggi, A.; Narbutovskih, M., Fracture testing of silicon microcantilever beams. *Journal of Applied Physics* **1996,** *79* (5), 2386-2393.

9. Kashyap, K.; Long-Chia, Z.; Dong-Yan, L.; Hou, M. T.; Yeh, J. A., Rollable silicon IC wafers achieved by backside nanotexturing. *IEEE Electron Device Letters* **2015,** *36* (8), 829-831.

10. Li, B.; Zhang, Y.; Fu, L.; Yu, T.; Zhou, S.; Zhang, L.; Yin, L., Surface passivation engineering strategy to fully-inorganic cubic CsPbI3 perovskites for high-performance solar cells. *Nature Communications* **2018,** *9* (1), 1076.

11. Noh, J. H.; Im, S. H.; Heo, J. H.; Mandal, T. N.; Seok, S. I., Chemical management for colorful, efficient, and stable inorganic-organic hybrid nanostructured solar cells. *Nano Letters* **2013,** *13* (4), 1764-9.

12. Saga, T., Advances in crystalline silicon solar cell technology for industrial mass production. *NPG Asia Materials* **2010,** *2* (3), 96-102.

13. Lee, H. S.; Choi, J. M.; Jung, B.; Kim, J.; Song, J.; Jeong, D. S.; Park, J. K.; Kim, W. M.; Lee, D. K.; Lee, T. S.; Lee, W. S.; Lee, K. S.; Ju, B. K.; Kim, I., Random nanohole arrays and its application to crystalline Si thin foils produced by proton induced exfoliation for solar cells. *Scientific Reports* **2019,** *9* (1), 19736.

14. Xue, M.; Nazif, K. N.; Lyu, Z.; Jiang, J.; Lu, C.-Y.; Lee, N.; Zang, K.; Chen, Y.; Zheng, T.; Kamins, T. I.; Brongersma, M. L.; Saraswat, K. C.; Harris, J. S., Free-standing 2.7 μm thick ultrathin crystalline silicon solar cell with efficiency above 12.0%. *Nano Energy* **2020,** *70*.

15. Burghartz, J. N.; Angelopoulos, E.; Appel, W.; Endler, S.; Ferwana, S.; Harendt, C.; Hassan, M. U.; Rempp, H.; Richter, H.; Zimmermann, M., Ultra-thin Si chips for flexible electronics process technology, characterization, assembly and applications. In *28th Symposium on Microelectronics Technology and Devices (SBMicro 2013)*, **2013;** pp 1-3.

16. Khang, D. Y.; Jiang, H.; Huang, Y.; Rogers, J. A., A stretchable form of single-crystal silicon for high-performance electronics on rubber substrates. *Science* **2006,** *311* (5758), 208-12.

17. Green, M. A., Silicon photovoltaic modules: a brief history of the first 50 years. *Progress in Photovoltaics: Research and Applications* **2005,** *13* (5), 447-455.

18. Campbell, P.; Green, M. A., High performance light trapping textures for monocrystalline silicon solar cells. *Solar Energy Materials and Solar Cells* **2001,** *65* (1-4), 369-375.

19. Kashyap, K.; Kumar, A.; Chen, C.-N.; Hou, M. T.; Yeh, J. A., Nanostructured silicon flapping wing with higher strength and low reflectivity for solar powered MEMS aircraft. In *2014 IEEE 27th International Conference on Micro Electro Mechanical Systems (MEMS)*, **2014**; pp 648-651.

20. Lin, C.-C.; Chuang, Y.-J.; Sun, W.-H.; Cheng, C.; Chen, Y.-T.; Chen, Z.-L.; Chien, C.-H.; Ko, F.-H., Ultrathin single-crystalline silicon solar cells for mechanically flexible and optimal surface morphology designs. *Microelectronic Engineering* **2015,** *145*, 128-132.

21. Munzer, K. A.; Holdermann, K. T.; Schlosser, R. E.; Sterk, S., Thin monocrystalline silicon solar cells. *IEEE Transactions on Electron Devices* **1999,** *46* (10), 2055-2061.

22. Seo, S.-W.; Chae, H.; Joon Seo, S.; Kyoon Chung, H.; Min Cho, S., Extremely bendable thin-film encapsulation of organic light-emitting diodes. *Applied Physics Letters* **2013,** *102* (16).

23. Kim, L. H.; Kim, K.; Park, S.; Jeong, Y. J.; Kim, H.; Chung, D. S.; Kim, S. H.; Park, C. E., Al_2O_3/TiO_2 nanolaminate thin film encapsulation for organic thin film transistors via plasma-enhanced

atomic layer deposition. *ACS Applied Materials & Interfaces* **2014,** *6* (9), 6731-8.

24. Steinmann, V.; Moro, L., Encapsulation requirements to enable stable organic ultra-thin and stretchable devices. *Journal of Materials Research* **2018,** *33* (13), 1925-1936.

25. Han, Y. C.; Kim, E.; Kim, W.; Im, H.-G.; Bae, B.-S.; Choi, K. C., A flexible moisture barrier comprised of a SiO_2-embedded organic–inorganic hybrid nanocomposite and Al_2O_3 for thin-film encapsulation of OLEDs. *Organic Electronics* **2013,** *14* (6), 1435-1440.

26. Seo, S.-W.; Jung, E.; Joon Seo, S.; Chae, H.; Kyoon Chung, H.; Min Cho, S., Toward fully flexible multilayer moisture-barriers for organic light-emitting diodes. *Journal of Applied Physics* **2013,** *114* (14).

27. Carcia, P. F.; McLean, R. S.; Reilly, M. H.; Groner, M. D.; George, S. M., Ca test of Al_2O_3 gas diffusion barriers grown by atomic layer deposition on polymers. *Applied Physics Letters* **2006,** *89* (3).

28. Mandlik, P.; Gartside, J.; Han, L.; Cheng, I. C.; Wagner, S.; Silvernail, J. A.; Ma, R.-Q.; Hack, M.; Brown, J. J., A single-layer permeation barrier for organic light-emitting displays. *Applied Physics Letters* **2008,** *92* (10).

29. Blakers, A. W.; Armour, T., Flexible silicon solar cells. *Solar Energy Materials and Solar Cells* **2009,** *93* (8), 1440-1443.

30. Dobrzański, L. A.; Drygała, A.; Gołombek, K.; Panek, P.; Bielańska, E.; Zięba, P., Laser surface treatment of multicrystalline silicon for enhancing optical properties. *Journal of Materials Processing Technology* **2008,** *201* (1-3), 291-296.

31. Lee, J.-S.; Kwon, S.-W.; Park, H.-Y.; Kim, Y.-D.; Kim, H.-J.; Lim, H.-J.; Yoon, S.-W.; Kim, D.-H., The flexural strengths of silicon substrates with various surface morphologies for silicon solar cells. *Korean Journal of Materials Research* **2009,** *19* (1), 18-23.

32. Sato, K.; Shikida, M.; Matsushima, Y.; Yamashiro, T.; Asaumi, K.; Iriye, Y.; Yamamoto, M., Characterization of orientation-dependent etching properties of single-crystal silicon: effects of KOH concentration. *Sensors and Actuators A: Physical* **1998,** *64* (1), 87-93.

33. Basu, P. K.; Sarangi, D.; Shetty, K. D.; Boreland, M. B., Liquid silicate additive for alkaline texturing of mono-Si wafers to improve process bath lifetime and reduce IPA consumption. *Solar Energy Materials and Solar Cells* **2013,** *113*, 37-43.

34. Jansen, H. V.; de Boer, M. J.; Ma, K.; Gironès, M.; Unnikrishnan, S.; Louwerse, M. C.; Elwenspoek, M. C., Black silicon method XI: oxygen pulses in SF6 plasma. *Journal of Micromechanics and Microengineering* **2010,** *20* (7).

35. Shirasawa, K., Mass production technology for multicrystalline Si solar cells. *Progress in Photovoltaics: Research and Applications* **2002,** *10* (2), 107-118.

36. Ruby, D. S.; Zaidi, S. H.; Narayanan, S.; Damiani, B. M.; Rohatgi, A., Rie-texturing of multicrystalline silicon solar cells. *Solar Energy Materials and Solar Cells* **2002,** *74* (1-4), 133-137.

37. Chen, W.; Liu, Y.; Yang, L.; Wu, J.; Chen, Q.; Zhao, Y.; Wang, Y.; Du, X., Difference in anisotropic etching characteristics of alkaline and copper based acid solutions for single-crystalline Si. *Scientific Reports* **2018,** *8* (1), 3408.

38. Kashyap, K.; Kumar, A.; Huang, C. T.; Lin, Y. Y.; Hou, M. T.; Andrew Yeh, J., Elimination of strength degrading effects caused by surface microdefect: a prevention achieved by silicon nanotexturing to avoid catastrophic brittle fracture. *Scientific Reports* **2015,** *5*, 10869.

39. Marks, M. R.; Hassan, Z.; Cheong, K. Y., Characterization methods for ultrathin wafer and die quality: a review. *IEEE Transactions on Components, Packaging and Manufacturing Technology* **2014,** *4* (12), 2042-2057.

40. Yeung, B.; Tien-Yu Tom, L., An overview of experimental methodologies and their applications for die strength measurement. *IEEE Transactions on Components and Packaging Technologies* **2003,** *26* (2), 423-428.

41. Min, Y.-K.; Byeon, J.-W., Evaluation of flexural strength of silicon die with thickness by 4 point bending test. In *Journal of the Microelectronics & Packaging Society*, **2011**; Vol. 18, pp 15-21.

42. Meyers, M. A.; Chawla, K. K., *Mechanical behavior of materials*. Cambridge university press: **2008**.

43. Kwon, J. H.; Jeong, E. G.; Jeon, Y.; Kim, D. G.; Lee, S.; Choi, K. C., Design of highly water resistant, impermeable, and flexible thin-film encapsulation based on inorganic/organic hybrid layers. *ACS Applied Materials & Interfaces* **2019,** *11* (3), 3251-3261.

44. Roberts, A. P.; Henry, B. M.; Sutton, A. P.; Grovenor, C. R. M.; Briggs, G. A. D.; Miyamoto, T.; Kano, M.; Tsukahara, Y.; Yanaka, M., Gas permeation in silicon-oxide/polymer (SiO_x/PET) barrier films: role of the oxide lattice, nano-defects and macro-defects. *Journal of Membrane Science* **2002,** *208* (1-2), 75-88.

45. Grossiord, N.; Kroon, J. M.; Andriessen, R.; Blom, P. W. M., Degradation mechanisms in organic photovoltaic devices. *Organic Electronics* **2012,** *13* (3), 432-456.

46. Hauch, J. A.; Schilinsky, P.; Choulis, S. A.; Rajoelson, S.; Brabec, C. J., The impact of water vapor transmission rate on the lifetime of flexible polymer solar cells. *Applied Physics Letters* **2008,** *93*

(10).

47. Lewis, J. S.; Weaver, M. S., Thin-film permeation-barrier technology for flexible organic light-emitting devices. *IEEE Journal of Selected Topics in Quantum Electronics* **2004,** *10* (1), 45-57.

48. Yu, D.; Yang, Y.-Q.; Chen, Z.; Tao, Y.; Liu, Y.-F., Recent progress on thin-film encapsulation technologies for organic electronic devices. *Optics Communications* **2016,** *362*, 43-49.

49. Lv, Y.; Xu, P.; Ren, G.; Chen, F.; Nan, H.; Liu, R.; Wang, D.; Tan, X.; Liu, X.; Zhang, H.; Chen, Z. K., Low-temperature atomic layer deposition of metal oxide layers for perovskite solar cells with high efficiency and stability under harsh environmental conditions. *ACS Applied Materials & Interfaces* **2018,** *10* (28), 23928-23937.

50. Dunkel, R.; Bujas, R.; Klein, A.; Horndt, V., A new method for measuring ultra-low water-vapor permeation for OLED displays. *Journal of the Society for Information Display* **2005,** *13* (7), 569-573.

51. Reese, M. O.; Dameron, A. A.; Kempe, M. D., Quantitative calcium resistivity based method for accurate and scalable water vapor transmission rate measurement. *Review of Scientific Instruments* **2011,** *82* (8), 085101.

52. Choi, J. H.; Kim, Y. M.; Park, Y. W.; Huh, J. W.; Ju, B. K.; Kim, I. S.; Hwang, H. N., Evaluation of gas permeation barrier properties using electrical measurements of calcium degradation. *Review of Scientific Instruments* **2007,** *78* (6), 064701.

53. Bertrand, J. A.; Higgs, D. J.; Young, M. J.; George, S. M., H_2O vapor transmission rate through polyethylene naphthalate polymer using the electrical Ca test. *The Journal of Physical Chemistry A* **2013,** *117* (46), 12026-34.

54. Schubert, S.; Klumbies, H.; Muller-Meskamp, L.; Leo, K., Electrical calcium test for moisture barrier evaluation for organic devices. *Review of Scientific Instruments* **2011,** *82* (9), 094101.

55. Bertrand, J. A.; George, S. M., Evaluating Al_2O_3 gas diffusion barriers grown directly on Ca films using atomic layer deposition techniques. *Journal of Vacuum Science & Technology A: Vacuum, Surfaces, and Films* **2013,** *31* (1).

56. Choi, M.-C.; Kim, Y.; Ha, C.-S., Polymers for flexible displays: From material selection to device applications. *Progress in Polymer Science* **2008,** *33* (6), 581-630.

57. Lewis, J., Material challenge for flexible organic devices. *Materials Today* **2006,** *9* (4), 38-45.

58. Park, S.-H. K.; Oh, J.; Hwang, C.-S.; Lee, J.-I.; Yang, Y. S.; Chu, H. Y., Ultrathin film encapsulation of an OLED by ALD. *Electrochemical and Solid-State Letters* **2005,** *8* (2).

59. Seethamraju, S.; Kumar, S.; B, K. B.; Madras, G.; Raghavan, S.; Ramamurthy, P. C., Million-fold decrease in polymer moisture permeability by a graphene monolayer. *ACS Nano* **2016,** *10* (7), 6501-9.

60. Kang, S. G.; Moon, D.; Jang, J.; Kim, J. Y.; Suh, J. Y.; Yoon, E.; Han, H. N.; Choi, I. S., Flaw-containing alumina hollow nanostructures have ultrahigh fracture strength to be incorporated into high-efficiency GaN light-emitting diodes. *Nano Letters* **2018,** *18* (2), 1323-1330.

61. Carter, C. B.; Norton, M. G., *Ceramic Materials*. **2013**.

62. Jang, D.; Meza, L. R.; Greer, F.; Greer, J. R., Fabrication and deformation of three-dimensional hollow ceramic nanostructures. *Nature Materials* **2013,** *12* (10), 893-8.

63. Gao, H.; Ji, B.; Jager, I. L.; Arzt, E.; Fratzl, P., Materials become insensitive to flaws at nanoscale: lessons from nature. *Proceedings of the National Academy of Science of the United States of America* **2003,** *100* (10), 5597-600.

64. Dameron, A. A.; Davidson, S. D.; Burton, B. B.; Carcia, P. F.; McLean, R. S.; George, S. M., Gas diffusion barriers on polymers using multilayers fabricated by Al_2O_3 and rapid SiO_2 atomic layer deposition. *The Journal of Physical Chemistry C* **2008,** *112* (12), 4573-4580.

65. George, S. M., Atomic layer deposition: an overview. *Chemical Reviews* **2010,** *110* (1), 111-31.

66. Johnson, R. W.; Hultqvist, A.; Bent, S. F., A brief review of atomic layer deposition: from fundamentals to applications. *Materials Today* **2014,** *17* (5), 236-246.

67. Groner, M. D.; Fabreguette, F. H.; Elam, J. W.; George, S. M., Low-temperature Al_2O_3 atomic layer deposition. *Chemistry of Materials* **2004,** *16* (4), 639-645.

68. Kim, S. K.; Lee, S. W.; Hwang, C. S.; Min, Y.-S.; Won, J. Y.; Jeong, J., Low temperature (<100° C) deposition of aluminum oxide thin films by ALD with O_3 as oxidant. *Journal of The Electrochemical Society* **2006,** *153* (5).

69. Heil, S. B. S.; Kudlacek, P.; Langereis, E.; Engeln, R.; van de Sanden, M. C. M.; Kessels, W. M. M., In situ reaction mechanism studies of plasma-assisted atomic layer deposition of Al_2O_3. *Applied Physics Letters* **2006,** *89* (13).

70. Yun, S. J.; Lim, J. W.; Lee, J.-H., Low-temperature deposition of aluminum oxide on polyethersulfone substrate using plasma-enhanced atomic layer deposition. *Electrochemical and Solid-State Letters* **2004,** *7* (1).

71. Wilson, C. A.; Grubbs, R. K.; George, S. M., Nucleation and growth during Al_2O_3 atomic layer deposition on polymers. *Chemistry of Materials* **2005,** *17* (23), 5625-5634.

72. Singh, P.; Jha, R. K.; Singh, R. K.; Singh, B. R., Preparation and characterization of Al_2O_3 film deposited by RF sputtering and plasma enhanced atomic layer deposition. *Journal of Vacuum Science & Technology B Nanotechnology and Microelectronics Materials Processing Measurement and Phenomena* **2018,** *36* (4).

73. Lee, S.; Choi, H.; Shin, S.; Park, J.; Ham, G.; Jung, H.; Jeon, H., Permeation barrier properties of an Al_2O_3/ZrO_2 multilayer deposited by remote plasma atomic layer deposition. *Current Applied Physics* **2014,** *14* (4), 552-557.

74. Nam, T.; Park, Y. J.; Lee, H.; Oh, I.-K.; Ahn, J.-H.; Cho, S. M.; Kim, H.; Lee, H.-B.-R., A composite layer of atomic-layer-deposited Al_2O_3 and graphene for flexible moisture barrier. *Carbon* **2017,** *116*, 553-561.

75. Schmidt, J.; Veith, B.; Werner, F.; Zielke, D.; Brendel, R., Photovoltaic Specialists Conference, 35th IEEE Honolulu. *HI USA, June* **2010**, 20-25.

76. Kwon, J. H.; Choi, S.; Jeon, Y.; Kim, H.; Chang, K. S.; Choi, K. C., Functional design of dielectric-metal-dielectric-based thin-film encapsulation with heat transfer and flexibility for flexible displays. *ACS Applied Materials & Interfaces* **2017,** *9* (32), 27062-27072.

77. Meyer, J.; Görrn, P.; Bertram, F.; Hamwi, S.; Winkler, T.; Johannes, H.-H.; Weimann, T.; Hinze, P.; Riedl, T.; Kowalsky, W., Al_2O_3/ZrO_2 nanolaminates as ultrahigh gas-diffusion barriers-a strategy for reliable encapsulation of organic electronics. *Advanced Materials* **2009,** *21* (18), 1845-1849.

78. Jang, J. H.; Kim, N.; Li, X.; An, T. K.; Kim, J.; Kim, S. H., Advanced thin gas barriers film incorporating alternating structure of PEALD-based Al_2O_3/organic-inorganic nanohybrid layers. *Applied Surface Science* **2019,** *475*, 926-933.

79. Ylivaara, O. M. E.; Liu, X.; Kilpi, L.; Lyytinen, J.; Schneider, D.; Laitinen, M.; Julin, J.; Ali, S.; Sintonen, S.; Berdova, M.; Haimi, E.; Sajavaara, T.; Ronkainen, H.; Lipsanen, H.; Koskinen, J.; Hannula, S.-P.; Puurunen, R. L., Aluminum oxide from trimethylaluminum and water by atomic layer deposition: the temperature dependence of residual stress, elastic modulus, hardness and adhesion. *Thin Solid Films* **2014,** *552*, 124-135.

80. Bauer, J.; Schroer, A.; Schwaiger, R.; Tesari, I.; Lange, C.; Valdevit, L.; Kraft, O., Push-to-pull tensile testing of ultra-strong nanoscale ceramic–polymer composites made by additive manufacturing. *Extreme Mechanics Letters* **2015,** *3*, 105-112.

81. van der Rest, A.; Idrissi, H.; Henry, F.; Favache, A.; Schryvers, D.; Proost, J.; Raskin, J.-P.; Van Overmeere, Q.; Pardoen, T., Mechanical behavior of ultrathin sputter deposited porous amorphous Al_2O_3 films. *Acta Materialia* **2017,** *125*, 27-37.

82. Borrero-López, O.; Vodenitcharova, T.; Hoffman, M., Anisotropy effects on the reliability of single-crystal silicon. *Scripta Materialia* **2010,** *63* (10), 997-1000.

83. Sánchez de la Morena, S.; Recio-Sánchez, G.; Torres-Costa, V.; Martín-Palma, R. J., Hybrid gold/porous silicon thin films for plasmonic solar cells. *Scripta Materialia* **2014,** *74*, 33-37.

84. Xue, C.; Huang, J.; Rao, J.; Varlamov, S., Fabrication of an ant-nest nanostructure in polycrystalline silicon thin films for solar cells. *Scripta Materialia* **2014,** *92*, 27-30.

85. Tavakoli, M. M.; Lin, Q.; Leung, S. F.; Lui, G. C.; Lu, H.; Li, L.; Xiang, B.; Fan, Z., Efficient, flexible and mechanically robust perovskite solar cells on inverted nanocone plastic substrates. *Nanoscale* **2016,** *8* (7), 4276-83.

86. Cheon, S. E.; Lee, H. S.; Choi, J.; Jeong, A. R.; Lee, T. S.; Jeong, D. S.; Lee, K. S.; Lee, W. S.; Kim, W. M.; Lee, H.; Kim, I., Fabrication of parabolic Si nanostructures by nanosphere lithography and its application for solar cells. *Scientific Reports* **2017,** *7* (1), 7336.

87. Boyce, B. L.; Shaw, M. J.; Lu, P.; Dugger, M. T., Stronger silicon for microsystems. *Acta Materialia* **2010,** *58* (2), 439-448.

88. Ćurković, L.; Bakić, A.; Kodvanj, J.; Haramina, T., Flexural strength of alumina ceramics: Weibull analysis. *Transactions of FAMENA* **2010,** *34* (1), 13-18.

89. Paul, I.; Majeed, B.; Razeeb, K.; Barton, J., Statistical fracture modelling of silicon with varying thickness. *Acta Materialia* **2006,** *54* (15), 3991-4000.

90. Pilkey, W. D.; Pilkey, D. F.; Bi, Z., *Peterson's stress concentration factors*. John Wiley & Sons: 2008.

91. Yeh, M.-K.; Shao, Y.-K.; Yeh, J. A.; Hsu, C., Stress distribution affected by nanostructures near a surface crack on a silicon chip. *Acta Mechanica* **2015,** *228* (8), 2791-2797.

92. Goel, S.; Kovalchenko, A.; Stukowski, A.; Cross, G., Influence of microstructure on the cutting behaviour of silicon. *Acta Materialia* **2016,** *105*, 464-478.

93. Vodenitcharova, T.; Borrero-López, O.; Hoffman, M., Mechanics prediction of the fracture pattern on scratching wafers of single crystal silicon. *Acta Materialia* **2012,** *60* (11), 4448-4460.

94. Zaitsu, S.-i.; Jitsuno, T.; Nakatsuka, M.; Yamanaka, T.; Motokoshi, S., Optical thin films

consisting of nanoscale laminated layers. *Applied Physics Letters* **2002,** *80* (14), 2442-2444.

95. Kukli, K.; Ritala, M.; Leskelä, M.; Jokinen, J., Atomic layer epitaxy growth of aluminum oxide thin films from a novel $Al(CH_3)_2Cl$ precursor and H_2O. *Journal of Vacuum Science & Technology A: Vacuum, Surfaces, and Films* **1997,** *15* (4), 2214-2218.

96. Lee, C.; Wei, X.; Kysar, J. W.; Hone, J., Measurement of the elastic properties and intrinsic strength of monolayer graphene. *Science* **2008,** *321* (5887), 385-8.

97. Zheng, K.; Wang, C.; Cheng, Y. Q.; Yue, Y.; Han, X.; Zhang, Z.; Shan, Z.; Mao, S. X.; Ye, M.; Yin, Y.; Ma, E., Electron-beam-assisted superplastic shaping of nanoscale amorphous silica. *Nature Communications* **2010,** *1*, 24.

98. Qu, X.; Deng, Q., Damage and recovery induced by a high energy e-beam in a silicon nanofilm. *RSC Advances* **2017,** *7* (59), 37032-37038.

99. Mačković, M.; Niekiel, F.; Wondraczek, L.; Bitzek, E.; Spiecker, E., In situ mechanical quenching of nanoscale silica spheres in the transmission electron microscope. *Scripta Materialia* **2016,** *121*, 70-74.

100. Zinkle, S. J.; Kinoshita, C., Defect production in ceramics. *Journal of Nuclear Materials* **1997,** *251*, 200-217.

101. Nakamura, R.; Ishimaru, M.; Yasuda, H.; Nakajima, H., Atomic rearrangements in amorphous Al2O3 under electron-beam irradiation. *Journal of Applied Physics* **2013,** *113* (6).

102. Tapily, K.; Jakes, J. E.; Stone, D. S.; Shrestha, P.; Gu, D.; Baumgart, H.; Elmustafa, A. A., Nanoindentation investigation of HfO_2 and Al_2O_3 films grown by atomic layer deposition. *Journal of The Electrochemical Society* **2008,** *155* (7).

103. Liu, X.; Haimi, E.; Hannula, S.-P.; Ylivaara, O. M. E.; Puurunen, R. L., On the reliability of nanoindentation hardness of Al_2O_3 films grown on Si-wafer by atomic layer deposition. *Journal of Vacuum Science & Technology A: Vacuum, Surfaces, and Films* **2014,** *32* (1).

104. Purkl, F.; Daus, A.; English, T. S.; Provine, J.; Feyh, A.; Urban, G.; Kenny, T. W., Measurement of Young′s modulus and residual stress of atomic layer deposited Al_2O_3 and Pt thin films. *Journal of Micromechanics and Microengineering* **2017,** *27* (8).

105. Tripp, M. K.; Stampfer, C.; Miller, D. C.; Helbling, T.; Herrmann, C. F.; Hierold, C.; Gall, K.; George, S. M.; Bright, V. M., The mechanical properties of atomic layer deposited alumina for use in micro- and nano-electromechanical systems. *Sensors and Actuators A: Physical* **2006,** *130-131*, 419-429.

106. Gu, X. W.; Wu, Z.; Zhang, Y. W.; Srolovitz, D. J.; Greer, J. R., Microstructure versus flaw: mechanisms of failure and strength in nanostructures. *Nano Letters* **2013,** *13* (11), 5703-9.

107. Suo, Z.; Ma, E. Y.; Gleskova, H.; Wagner, S., Mechanics of rollable and foldable film-on-foil electronics. *Applied Physics Letters* **1999,** *74* (8), 1177-1179.

108. Bonamy, D.; Prades, S.; Rountree, C. L.; Ponson, L.; Dalmas, D.; Bouchaud, E.; Ravi-Chandar, K.; Guillot, C., Nanoscale damage during fracture in silica glass. *International Journal of Fracture* **2006,** *140* (1-4), 3-14.

109. Luo, J.; Wang, J.; Bitzek, E.; Huang, J. Y.; Zheng, H.; Tong, L.; Yang, Q.; Li, J.; Mao, S. X., Size-dependent brittle-to-ductile transition in silica glass nanofibers. *Nano Letters* **2016,** *16* (1), 105-13.

110. Bonfanti, S.; Ferrero, E. E.; Sellerio, A. L.; Guerra, R.; Zapperi, S., Damage accumulation in silica glass nanofibers. *Nano Letters* **2018,** *18* (7), 4100-4106.

111. Frankberg, E. J.; Kalikka, J.; Garcia Ferre, F.; Joly-Pottuz, L.; Salminen, T.; Hintikka, J.; Hokka, M.; Koneti, S.; Douillard, T.; Le Saint, B.; Kreiml, P.; Cordill, M. J.; Epicier, T.; Stauffer, D.; Vanazzi, M.; Roiban, L.; Akola, J.; Di Fonzo, F.; Levanen, E.; Masenelli-Varlot, K., Highly ductile amorphous oxide at room temperature and high strain rate. *Science* **2019,** *366* (6467), 864-869.

112. Patel, R. P.; Wolden, C. A., Defect analysis and mechanical performance of plasma-deposited thin films on flexible polycarbonate substrates. *Applied Surface Science* **2013,** *268*, 416-424.

113. Zhao, J.; Cai, B.; Luo, Z.; Dong, Y.; Zhang, Y.; Xu, H.; Hong, B.; Yang, Y.; Li, L.; Zhang, W.; Gao, C., Investigation of the hydrolysis of perovskite organometallic halide $CH_3NH_3PbI_3$ in humidity environment. *Scientific Reports* **2016,** *6*, 21976.

114. Yang, J.; Siempelkamp, B. D.; Liu, D.; Kelly, T. L., Investigation of $CH_3NH_3PbI_3$ degradation rates and mechanisms in controlled humidity environments using in situ techniques. *ACS Nano* **2015,** *9* (2), 1955-63.

115. Zhang, C.-X.; Shen, T.; Guo, D.; Tang, L.-M.; Yang, K.; Deng, H.-X., Reviewing and understanding the stability mechanism of halide perovskite solar cells. *InfoMat* **2020**.